Multi-species flow indirect-noise modeling re-examined with a helicopter-engine application

Y. Gentil* and G. Daviller†
CERFACS, 42 Avenue Gaspard Coriolis, Toulouse, 31057, France

S. Moreau‡
University of Sherbrooke, Sherbrooke, J1K2R1, QC, Canada

T. Poinsot§
Toulouse Institute of Fluid Mechanics, Toulouse, 31400 France

Composition noise has recently received increasing attention for its potential to contribute significantly to the indirect noise mechanism. In this study, the importance and definition of composition noise are revisited by proposing a new proper decomposition between entropy and mixture compositional fluctuations. When assuming quasi one-dimensional, multi-species, isentropic and non-reactive flow in nozzles, the resulting system of equations shows a new and remarkable one-way coupling between composition waves and both acoustic and entropy waves. Relying on the Magnus-expansion methodology, an exact solution of that system is investigated. The proposed theory is validated by comparing the model predictions with direct numerical simulation of nozzle flows in which compositional fluctuations are pulsed. It is shown that composition transfer functions from the unsteady simulations are in agreement with the analytical model of this paper. Finally, a hybrid approach is investigated consisting of extracting waves from a Large-Eddy Simulation (LES) of a real helicopter engine and propagating those through different nozzle geometries. Composition noise is found negligible compared to direct or indirect entropy noise since it is at least 20 dB lower than other noise mechanisms for all tested cases.

I. Nomenclature

ρ =   density, kg/m^3

u =   axial speed, m/s

$\tilde{u}$ =   dimensionless axial speed

A	=	nozzle cross-section, m^2
p	=	pressure, Pa
$p°$	=	reference pressure, Pa
P_t	=	total pressure, Pa
T	=	temperature, K
$T°$	=	reference temperature, K
T_t	=	total temperature, K
$\mathcal{R}_u$	=	universal gas constant, $J/(K \cdot mol)$
s	=	specific entropy of a mixture, J/(kg $\cdot$ K)
W	=	mean molar mass of a mixture, kg/mol
r	=	specific gas constant of a mixture, J/(kg $\cdot$ K)
h	=	specific enthalpy of a mixture, J/kg
h_t	=	total specific enthalpy, J/kg
C_p	=	specific heat capacity of a mixture, J/(kg $\cdot$ K)
M	=	axial Mach number
c	=	sound speed, m/s
ϕ	=	mixture equivalence ratio
c	=	sound speed, m/s
Y_i	=	species mass fraction of the i-th species
X_i	=	species molar fraction of the i-th species
W_i	=	molar mass of the i-th species, kg/mol
r_i	=	specific gas constant of the i-th species, J/(kg $\cdot$ K)
$\tilde{G}_i$	=	partial molar Gibbs' energy of the i-th species, J/mol
μ_i	=	chemical potential of the i-th species, J/mol
γ	=	adiabatic index
$C_{p,i}$	=	specific heat capacity of the i-th species, J/(kg $\cdot$ K)
s_i	=	specific entropy of the i-th species, J/(kg $\cdot$ K)
h_i	=	specific enthalpy of the i-th species, J/kg
N	=	the number of considered species
Z	=	mixture-fraction space variable
x	=	axial coordinate, m
y	=	transverse coordinate, m

ξ	=	dimensionless axial coordinate
L_n	=	nozzle axial length, m
θ	=	angular coordinate
R	=	radius coordinate, m
t	=	time variable, s
τ	=	dimensionless time variable
T_{sim}	=	simulation time, s
f	=	perturbation frequency, Hz
ω	=	perturbation pulsation
Ω	=	Helmholtz number
m	=	azimuthal wave number
K_x	=	dimensionless axial wave number
w^+	=	downstream-propagating acoustic wave
w^-	=	upstream-propagating acoustic wave
w^s	=	entropy wave
w^z	=	compositional wave
W_{ref}	=	reference sound speed, W
$I_{dB/Hz}$	=	acoustic intensity levels, dB/Hz
I_{dB}	=	total acoustic intensity, dB
a_{conv}	=	angle of the nozzle convergent relatively to the x-axis
a_{div}	=	angle of the nozzle divergent relatively to the x-axis
R^-	=	composition-to-acoustic reflection transfer function
T^+	=	composition-to-acoustic (w^+) transmission transfer function
T^-	=	composition-to-acoustic (w^-)transmission transfer function
T^s	=	composition-to-entropy transmission transfer function
T^z	=	composition-to-composition transmission transfer function
T_z^+	=	composition-to-acoustic (w^+) transmission transfer function
T_s^+	=	entropy-to-acoustic (w^+) transmission transfer function
T_+^+	=	acoustic-to-acoustic (w^+)transmission transfer function
T_z^-	=	composition-to-acoustic (w^-)transmission transfer function
T_s^-	=	entropy-to-acoustic (w^-) transmission transfer function
T_+^-	=	acoustic-to-acoustic (w^-) transmission transfer function

II. Introduction

Combustion noise is an increasing contributor to overall aircraft-noise [1–3].

Initially produced within the combustion chamber by heat-release fluctuations of the flame, the noise is then successively transmitted through the turbine and is referred to as *direct combustion noise*. Nevertheless, three other types of inhomogeneities are produced within the combustion chamber: entropy spots, vortical and compositional inhomogeneities; they can generate noise when being propagated through the non-uniform flow of the turbine stages. These three mechanisms, commonly referred to as *indirect combustion noise*, can in some instances overcome the first mechanism according to [2, 3]. The propagation of entropy spots and vortical inhomogeneities have been extensively investigated in the past [4–7] whilst assuming homogeneous composition mixture. Nevertheless, the flow downstream of the combustion chamber is usually inhomogeneous not only in entropy and vorticity but also in species due to several mechanisms such as turbulence, dilution or film cooling. Consequently, as the flow moves through the turbine stages, the homogeneous composition mixture assumption may not be necessarily apt. Indeed, compositional fluctuations may contribute to the *indirect combustion noise* mechanism, as recently mentioned in [8, 9].

On the one hand, using a hybrid framework consisting of unsteady combustion LES coupled to low-order nozzle simulation, Shao *et al.* [10] found comparable indirect noise contributions between composition and entropy waves near lean blow-out operating conditions. On the other hand, simulating a realistic rich-quench-lean (RQL) combustor coupled with a nozzle guide vane with LES, Giusti *et al.* [11] tracked the formation and evolution of composition and temperature inhomogeneities, and subsequently the different noise generation mechanisms. As a result, indirect noise generated by temperature fluctuations was found to be larger than indirect noise generated by compositional fluctuations despite significant composition and temperature fluctuations found at the combustor exit. Furthermore, the combustion noise prediction methodology [2, 3], called CONOCHAIN for COmbustion NOise CHAIN, showed fair agreement with experiments without considering composition noise. Finally, Lapeyre [12] observed that indirect composition noise is generated only when a change of density is produced. Nevertheless, this change of density is already taken into account through the "excess-density" wave defined for homogeneous species flow as the entropy wave. Up to now, there is no clear consensus on the importance of composition noise, and contradictory results on its relevance have been reported so far.

The present article shows that this may be caused by the incomplete prediction of composition-to-acoustic transfer function, as a result of the considered wave decomposition vector of the Magri-O'Brien-Ihme (MOI) model [8–11, 13, 14] In the latter model, the common wave decomposition vector is given by the two acoustic waves w^+ and w^- (traveling upstream and downstream, respectively), the entropy wave w^s and the composition wave w^z. According to this decomposition, the entropy wave is assumed to propagate independently of the composition wave. Nevertheless, this entropy wave varies with temperature fluctuations but also with compositional fluctuations as clarified in section III. Therefore, by pulsing compositional fluctuation meanwhile ensuring zero entropy fluctuation at the nozzle inlet leads

to incomplete composition transfer function calculation. In order to correctly predict the composition-to-acoustic transfer functions, the pulsation of composition waves and its associated entropy wave is required. To do so, a new wave decomposition basis is introduced in this work to properly separate the contributions due to temperature fluctuations and to compositional fluctuations.

The aim of the present study is therefore to more precisely describe the composition noise mechanism and investigate its potential to contribute significantly to the overall noise. To begin with, the mathematical model describing the propagation of waves within the nozzle is presented in section III. Relying on the Magnus expansion method [5, 15], an exact solution of the resulting system of linearized Euler equations is proposed in section IV. The model is then validated comparing the exact solution with unsteady simulations in section V, providing the extension of the Navier-Stokes Characteristics Boundary Conditions (NSCBC) methodology to multi-species flow shown in section Appendix B. Two test cases deal with different burning gas mixtures and different nozzle flow regimes. The first test case (kerosene-air) provides the validation of the model with direct numerical simulations for subsonic and choked flows. For the second test case, the composition-to-acoustic transfer functions are evaluated in the similar framework as in [13] (methane-air, choked flow) and compared with results from an unsteady simulation and from the model presented in this paper. Finally, an application to a real engine is proposed in section VI consisting of extracting waves from the Large Eddy Simulation of the TEENI combustion chamber [16] and propagating them through variable geometry nozzles, allowing parametric investigation of noise mechanisms.

III. Noise mechanism through isentropic and multi-species nozzle flow

Assuming the flow to be multi-species, adiabatic, chemically frozen, calorifically perfect, at high Reynolds number, reversible and thus isentropic, quasi-one dimensional (i.e. the nozzle cross-section $A(x)$ in figure 1 varies slowly with the axial coordinate x and the variations of velocity only occur in this direction), the conservation equations [17] reduce to the quasi-one dimensional Euler equations given by:

$$\frac{D\rho}{Dt} + \rho \frac{\partial u}{\partial x} = -\frac{\rho u}{A}\frac{\partial A}{\partial x}, \qquad \rho \frac{Du}{Dt} + \frac{\partial p}{\partial x} = 0, \qquad \frac{Ds}{Dt} = 0, \qquad \frac{DY_i}{Dt} = 0 \qquad \text{and} \qquad p = \rho \frac{\mathcal{R}_u}{W}T = \rho \, r \, T \quad (1)$$

where the substantial derivative is defined as $\dfrac{D}{Dt} = \dfrac{\partial}{\partial t} + u\dfrac{\partial}{\partial x}$; ρ, u, p and T are the fluid density, the axial velocity, the static pressure and the static temperature respectively; s is the specific entropy; Y_i and W_i are the mass fractions and the molar mass of the ith species respectively; N is the total number of species; $\mathcal{R}_u$ is the universal gas constant and W is the mean molar mass such that: $1/W = \sum_{i=1}^{N} Y_i/W_i$.

Furthermore, Gibbs' equation for multi-species flow gives the following definition of the specific entropy:

$$T ds = dh - \frac{dp}{\rho} - \sum_{i=1}^{N} \frac{\tilde{G}_i}{W_i} dY_i \equiv dh - \frac{dp}{\rho} - \sum_{i=1}^{N} \frac{\mu_i}{W_i} dY_i \tag{2}$$
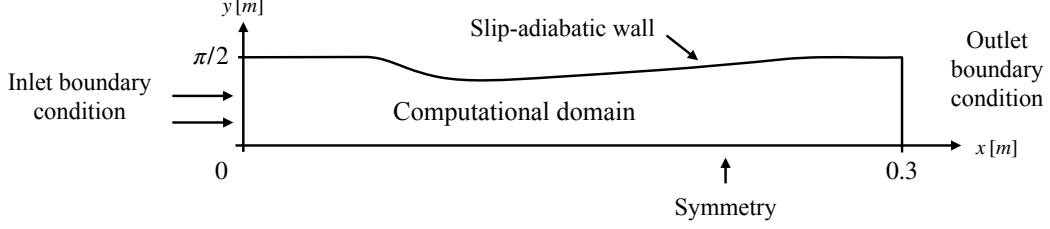
Fig. 1 Axisymmetric nozzle domain (x,y) with boundary conditions.

where h and s are the specific enthalpy and entropy respectively, $\tilde{G}_i$ is the partial molar Gibbs' energy of the i-th species and μ_i is the chemical potential ($\tilde{G}_i \equiv \mu_i$).

Note that when considering an heterogeneous species mixture flow, the specific entropy and enthalpy of a calorifically perfect gas mixture are provided, according to [18], by:

$$s = \sum_{i=1}^{N} \left(s_i(T, p) - r_i \ln(X_i) \right) Y_i \quad \text{where} \quad s_i(T, p) = C_{p,i} \log\left(\frac{T}{T^\circ} \right) - r_i \log\left(\frac{p}{p^\circ} \right) \tag{3a}$$

$$h = \sum_{i=1}^{N} h_i Y_i \qquad \text{where} \quad h_i(T) = C_{p,i}(T - T^\circ) \tag{3b}$$

Considering only the mean steady flow, the quasi-1D Euler equations (1) reduce to:

$$\frac{\partial \bar{\rho}\bar{u}A}{\partial x} = 0, \quad \bar{u}\frac{\partial \bar{u}}{\partial x} + \frac{1}{\bar{\rho}}\frac{\partial \bar{p}}{\partial x} = 0, \quad \bar{u}\frac{\partial \bar{Y}_i}{\partial x} = 0, \quad \bar{u}\frac{\partial \bar{s}}{\partial x} = 0 \tag{4}$$

where ($\bar{}$) represents the steady mean flow.

Assuming small dimensionless fluctuations noted (^) around the steady mean flow, the quasi-1D Euler equations are linearized by considering variables as follows:

$$\rho = \bar{\rho}(1 + \hat{\rho}), \quad p = \bar{p}(1 + \bar{\gamma}\hat{p}), \quad u = \bar{u}(1 + \hat{u}), \quad Y_i = \bar{Y}_i + \hat{Y}_i,$$

$$s_i = \bar{s}_i + \bar{C}_{p,i}\hat{s}_i, \quad r = \bar{r}(1 + \hat{r}), \quad C_p = \bar{C}_p(1 + \hat{C}_p), \quad T = \bar{T}(1 + \hat{T}), \tag{5}$$

$$s = \bar{s} + \bar{C}_p\hat{s}, \qquad C_{p,i} = \bar{C}_{p,i}, \qquad \gamma = \bar{\gamma} + \hat{\gamma}$$

Note here that the fluctuations can also be written in dimensional form using the notation $()'$ like for instance for the density fluctuations noted ρ'.

Introducing the mean equations (4) in equation (2) and taking the substantial derivative along a streamline, Gibbs'

energy equation becomes:

$$\left[\frac{\partial}{\partial t} + \bar{u}\frac{\partial}{\partial x} \right] \left((1 - \bar{\gamma})\hat{p} + \hat{T} + \log(2 + (\bar{\gamma} - 1)\bar{M}^2) \left[\sum_{i=1}^{N} \left(\frac{\bar{W}}{W_i} - \frac{\bar{C}_{p,i}}{\bar{C}_p} \right) \hat{Y}_i \right] \right) = 0 \tag{6}$$

where $\bar{M} = \bar{u}/\bar{c}$ is the mean axial Mach number.

When considering homogeneous species mixture flow, the following decomposition basis was used by Duran & Moreau [5]: $[\hat{p}, \hat{u}, \hat{s}]$ where $\hat{s} = \hat{T} + (1 - \bar{\gamma})\hat{p} = \hat{p} - \hat{\rho}$. When considering an heterogeneous species mixture flow, the linearization of the specific entropy (equation 3a) is extended with terms related to species mass fractions $\hat{Y}_i$ as follows:

$$\hat{s} = \underbrace{\sum_{i=1}^{N} \frac{\overline{C_{p,i}}}{\bar{C}_p} \bar{Y}_i \hat{s}_i}_{(1)} + \underbrace{\frac{1}{\bar{C}_p} \sum_{i=1}^{N} \left(\bar{s}_i - r_i \ln(\bar{X}_i) \right) \hat{Y}_i}_{(2)} \tag{7}$$

When linearizing the specific entropy of the i-th species noted s_i provided in equation (3a), the term (1) in equation (7) reduces to:

$$\sum_{i=1}^{N} \frac{\overline{C_{p,i}}}{\bar{C}_p} \bar{Y}_i \hat{s}_i = \hat{T} + (1 - \bar{\gamma})\hat{p} \tag{8}$$

Thereafter, a proper entropy fluctuation is defined and noted $\hat{s}_n$ such that $\hat{s}_n = \hat{T} + (1 - \bar{\gamma})\hat{p} \neq \hat{p} - \hat{\rho}$, which is independent of the mixture compositional fluctuations.

For simplicity, the dimensionless mixture fraction space fluctuation $\hat{Z}$ is introduced and the species mass-fractions fluctuations $\hat{Y}_i$ can be linked to $\hat{Z}$ using the first order derivation such that:

$$\hat{Y}_i = \frac{dY_i}{dZ}\hat{Z} \quad \text{and} \quad \left[\frac{\partial}{\partial t} + \bar{u}\frac{\partial}{\partial x} \right] \hat{Z} = 0 \tag{9}$$

Note that it is also possible to introduce the equivalence ratio fluctuation $\hat{\phi}$ instead or any relevant fluctuation quantity that ensures a proportional link between its variation and the species mass fractions fluctuations $\hat{Y}_i$.

Introducing the dimensionless fluctuation $\hat{s}_n$ and the mixture fraction space fluctuation $\hat{Z}$ into the conservation equations (1) and using equations (6), (9), the quasi-one dimensional linearized Euler Equations for non-reacting and

multi-species flow reads:

$$\left[\frac{\partial}{\partial t} + \bar{u}\frac{\partial}{\partial x}\right][\hat{p} - \hat{s}_n] + \bar{u}\frac{\partial \hat{u}}{\partial x} = 0, \tag{10a}$$

$$\left[\frac{\partial}{\partial t} + \bar{u}\frac{\partial}{\partial x}\right]\hat{u} + \frac{\bar{c}^2}{\bar{u}}\frac{\partial \hat{p}}{\partial x} + \left(2\hat{u} - (\bar{\gamma} - 1)\hat{p} - \hat{s}_n - \Lambda\hat{Z}\right)\frac{\partial \bar{u}}{\partial x} = 0, \tag{10b}$$

$$\left[\frac{\partial}{\partial t} + \bar{u}\frac{\partial}{\partial x}\right]\left(\hat{s}_n + \log(2 + (\bar{\gamma} - 1)\bar{M}^2)(\Lambda - \chi)\hat{Z}\right) = 0, \tag{10c}$$

$$\left[\frac{\partial}{\partial t} + \bar{u}\frac{\partial}{\partial x}\right]\hat{Z} = 0 \tag{10d}$$

where

$$\Lambda = \sum_{i=1}^{N}\frac{W}{W_i}\frac{\mathrm{d}Y_i}{\mathrm{d}Z} \quad \text{and} \quad \chi = \sum_{i=1}^{N}\frac{\bar{C}_{p,i}}{\bar{C}_p}\frac{\mathrm{d}Y_i}{\mathrm{d}Z} \tag{11}$$

When the mean flow gradient is set to zero (homogeneous flow), i.e. $\mathrm{d}\bar{u}/dx = 0$, four decoupled equations, called the characteristic equations, are obtained for the multi-species flow:

$$\left[\frac{\partial}{\partial t} + (\bar{u} + \bar{c})\frac{\partial}{\partial x}\right]w^+ = 0, \quad \left[\frac{\partial}{\partial t} + (\bar{u} - \bar{c})\frac{\partial}{\partial x}\right]w^- = 0, \quad \left[\frac{\partial}{\partial t} + \bar{u}\frac{\partial}{\partial x}\right]w_h^s = 0 \quad \text{and} \quad \left[\frac{\partial}{\partial t} + \bar{u}\frac{\partial}{\partial x}\right]w^z = 0 \tag{12}$$

where:

$$w^+ = \hat{p} + \bar{M}\hat{u}, \qquad w^- = \hat{p} - \bar{M}\hat{u}, \qquad w_h^s = \hat{s}_n \qquad \text{and} \qquad w^z = \hat{Z} \tag{13}$$

According to the characteristic equations (12), the *waves* are given by: $\left[w^+, w^-, w_h^s, w^z\right]$ and propagate at the convection speed: $\bar{u} + \bar{c}$, $\bar{u} - \bar{c}$, $\bar{u}$ and $\bar{u}$ respectively. Note that the independent entropy wave w_h^s is characterized for multi-species flow by the properly defined entropy fluctuation $\hat{s}_n$. In addition, these wave definitions are consistent with Duran & Moreau [5] when assuming homogeneous mixture flow, i.e $\hat{Z} = 0$.

When the mean flow gradient is different from zero, i.e. $\mathrm{d}\bar{u}/dx \neq 0$, it couples the four waves:

$$\left[\frac{\partial}{\partial t} + (\bar{u} + \bar{c})\frac{\partial}{\partial x}\right]w^+ = \left\{\frac{\eta^+ - \zeta\alpha^-}{\bar{M}}w^+ - \frac{\eta^+ - \zeta\alpha^+}{\bar{M}}w^- + \zeta w_h^s + \zeta\Gamma^- w^z\right\}\bar{u}\frac{\mathrm{d}\bar{M}}{\mathrm{d}x} \tag{14a}$$

$$\left[\frac{\partial}{\partial t} + (\bar{u} - \bar{c})\frac{\partial}{\partial x}\right]w^- = \left\{\frac{\zeta\alpha^- - \eta^-}{\bar{M}}w^+ + \frac{\eta^- - \zeta\alpha^+}{\bar{M}}w^- - \zeta w_h^s - \zeta\Gamma^+ w^z\right\}\bar{u}\frac{\mathrm{d}\bar{M}}{\mathrm{d}x} \tag{14b}$$

$$\left[\frac{\partial}{\partial t} + \bar{u}\frac{\partial}{\partial x}\right]w_h^s = -\left\{(\Lambda - \chi)\zeta(\gamma - 1)\bar{M}w^z\right\}\bar{u}\frac{\mathrm{d}\bar{M}}{\mathrm{d}x} \tag{14c}$$

$$\left[\frac{\partial}{\partial t} + \bar{u}\frac{\partial}{\partial x}\right]w^z = 0 \tag{14d}$$

8

where

$$\eta^{\pm} = \frac{1}{2}\left(1 \pm \frac{1}{\bar{M}}\right), \qquad \alpha^{\pm} = 1 \pm \frac{(\bar{\gamma} - 1)}{2}\bar{M}, \qquad \zeta = \left(1 + \frac{\bar{\gamma} - 1}{2}\bar{M}^2\right)^{-1} \quad \text{and} \quad \Gamma^{\pm} = \Lambda \pm (\Lambda - \chi)(\bar{\gamma} - 1)\bar{M}$$

Equations (14) describe how the waves (i.e fluctuations) propagate through an isentropic and non-reacting flow within a nozzle. Two mechanisms responsible for indirect noise generation are identified through the non-zero mean flow gradient term $d\bar{M}/dx$ and called *indirect entropy noise* and *indirect composition noise*. On the one hand, the first coupling mechanism involving the entropy wave w_h^s has been extensively investigated when assuming homogeneous mixture flows [5, 19, 20]. In the context of heterogeneous species mixture flow, this mechanism is similar and described by a one-way coupling between the entropy wave w_h^s and the acoustics waves (w^+, w^-). On the other hand, the *indirect composition noise* is produced by the acceleration/deceleration of the composition wave w^z, or equivalently the compositional fluctuations $\hat{Y}_i$, which has been investigated in [8–10, 13]. Furthermore, a new one-way coupling between the composition wave w^z and the entropy waves w_h^s is found here according to the equation (14c), which extends the existing MOI model [8]. Differences with the latter model are highlighted in Appendix A.

IV. Analytical solution

Based on the Magnus-expansion method [15], an exact solution of the system of equations is developed in the following. To do so, new invariants are introduced and are given by:

$$I_A = \left(\frac{\dot{m}'}{\bar{\dot{m}}}\right) = \hat{p} + \hat{u} - \hat{s}_n - \Lambda\hat{Z}, \tag{15a}$$

$$I_B = \left(\frac{h_t'}{\bar{h}_t}\right) = \zeta\left(\chi\hat{Z} + \hat{s}_n + (\bar{\gamma} - 1)\hat{p} + (\bar{\gamma} - 1)\bar{M}^2\hat{u}\right), \tag{15b}$$

$$I_C = \hat{s}_n + \log(2 + (\gamma - 1)M^2)(\Lambda - \chi)\hat{Z}, \tag{15c}$$

$$I_D = (Z') = \hat{Z} \tag{15d}$$

Note here that the invariant I_C is chosen relatively to equation (10c). In addition, since the product $\Lambda\hat{Z}$ is conserved, the invariant I_A is reduced to another invariant noted I_A^* such that: $I_A^* = \hat{p} + \hat{u} - \hat{s}_n$.

Introducing the dimensionless spaces and times variables: $\xi = x/L_n$ and $\tau = tf$, where L_n is the nozzle length and f is the characteristic frequency of the perturbation and the Helmholtz number $\Omega = fL_n/\bar{c}_0$, the equations (10) can be

recast into an invariant formulation following the procedure described in [5] such that:

$$\left[\Omega\frac{\partial}{\partial\tau} + \tilde{u}\frac{\partial}{\partial\xi}\right]I_A^* = \frac{\tilde{u}}{(\bar{\gamma}-1)\bar{M}^2}\left[\frac{\partial I_C}{\partial\xi} - \frac{1}{\zeta}\frac{\partial I_B}{\partial\xi} + \left(\chi - (\Lambda - \chi)\log(2 + (\bar{\gamma}-1)\bar{M}^2)\right)\frac{\partial I_D}{\partial\xi}\right] \tag{16a}$$

$$\left[\Omega\frac{\partial}{\partial\tau} + \tilde{u}\frac{\partial}{\partial\xi}\right]I_B = -\frac{(\bar{\gamma}-1)\tilde{u}}{\zeta}\left(\frac{\partial I_A^*}{\partial\xi} + \frac{\partial I_C}{\partial\xi} - \log(2 + (\bar{\gamma}-1)\bar{M}^2)(\Lambda - \chi)\frac{\partial I_D}{\partial\xi}\right) \tag{16b}$$

$$\left[\Omega\frac{\partial}{\partial\tau} + \tilde{u}\frac{\partial}{\partial\xi}\right]I_C = 0 \tag{16c}$$

$$\left[\Omega\frac{\partial}{\partial\tau} + \tilde{u}\frac{\partial}{\partial\xi}\right]I_D = 0 \tag{16d}$$

where the mean flow velocity $\bar{u}$ is noted $\tilde{u}$ and made dimensionless using the inlet sound speed $\bar{c}_0$ and the substantial derivative is defined as $\dfrac{D_0}{D_0\tau} = \Omega\dfrac{\partial}{\partial\tau} + \tilde{u}\dfrac{\partial}{\partial\xi}$.

Assuming the invariants to be harmonic, the system of equations can be recast into a matrix formulation as follows:

$$[E(\xi)]\frac{d}{d\xi}[I] = 2\pi i\Omega I \tag{17}$$

where $I = \left[I_A^*, I_B, I_C, I_D\right]$ is the vector of invariants and $E(\xi)$ is a non-constant 4×4 matrix:

$$E = -\tilde{u}\begin{bmatrix} 1 & \dfrac{1}{\zeta(\bar{\gamma}-1)\bar{M}^2} & -\dfrac{1}{(\bar{\gamma}-1)\bar{M}^2} & -\dfrac{\chi - (\Lambda - \chi)\log(2 + (\bar{\gamma}-1)\bar{M}^2)}{(\bar{\gamma}-1)\bar{M}^2} \\ (\bar{\gamma}-1)\zeta & 1 & (\bar{\gamma}-1)\zeta & -(\bar{\gamma}-1)\zeta(\Lambda - \chi)\log(2 + (\bar{\gamma}-1)\bar{M}^2) \\ 0 & 0 & 1 & 0 \\ 0 & 0 & 0 & 1 \end{bmatrix} \tag{18}$$

When the matrix E is invertible ($M \neq 1$), the system of equations finally reads:

$$\frac{d}{d\xi}[I] = \frac{-2\pi i\Omega}{\tilde{u}(\bar{M}^2 - 1)}[A(\xi)]I \tag{19}$$

where the matrix A is given by:

$$A = \begin{bmatrix} & & & \dfrac{\chi - \bar{\gamma}(\Lambda - \chi)\log(\nu)}{(\bar{\gamma}-1)} \\ & A_{3,3} & & \zeta\left(-\chi + (\Lambda - \chi)\log(\nu)(1 + (\bar{\gamma}-1)\bar{M}^2)\right) \\ & & & 0 \\ 0 & 0 & 0 & \bar{M}^2 - 1 \end{bmatrix} \tag{20}$$

where $\nu = 2 + (\bar{\gamma} - 1)\bar{M}^2$ and $A_{3,3}$ corresponds to the matrix formulated in [5]:

$$A_{3,3} = \begin{bmatrix} \bar{M}^2 & -\dfrac{1}{(\bar{\gamma}-1)\zeta} & \dfrac{\bar{\gamma}}{\bar{\gamma}-1} \\ -(\bar{\gamma}-1)\bar{M}^2\zeta & \bar{M}^2 & -\zeta\left(1+(\bar{\gamma}-1)\bar{M}^2\right) \\ 0 & 0 & \bar{M}^2-1 \end{bmatrix} \tag{21}$$

The system of equations (19) can be solved following the methodology extensively described in [5] depending on the flow conditions. Thereafter, the composition transfer functions are computed and defined as follows:

$$R^- = \frac{w_{in}^-}{w_{in}^z}, \qquad T^+ = \frac{w_{out}^+}{w_{in}^z}, \qquad T^- = \frac{w_{out}^-}{w_{in}^z} \qquad \text{and} \qquad T^s = \frac{w_{h,out}^s}{w_{in}^z} \tag{22}$$

where the subscripts $_{in}$ and $_{out}$ correspond to nozzle inlet and outlet values, respectively.

In the following, these transfer functions are termed *Non-Compact*.

V. Model validation and results

To validate the previous theory and solution, direct numerical simulations of 2D axisymmetric nozzle with different flows are performed thereafter with superimposed composition planar waves. The unstructured and massively parallel solver AVBP [21] is used to solve the Euler equations with the Lax-Wendroff scheme in the axisymmetric nozzle sketched in figure 1. The inlet and outlet boundary conditions are handled using the extended Navier-Stokes Characteristic Boundary Conditions (NSCBC), described in Appendix B, while a slip wall and a symmetry boundary condition are imposed on the upper nozzle wall and on the lower segment respectively. In addition, compositional fluctuations of different amplitudes depending on the considered gas mixture are pulsed at the inlet with frequencies ranging from 200 Hz to 6000 Hz every 100 Hz. For all simulations, the flow is initialized with steady mean flows and the CFL number is fixed to 0.7 to yield stability of the Lax-Wendroff convection scheme.

The first test case deals with the prediction of the indirect composition noise through two nozzle flow regimes: subsonic and choked. To do so, compositional fluctuations are assumed to be produced by equivalence ratio fluctuations of a kerosene-air mixture upstream of a front flame. Following the framework in [13], the second test case is performed to compare the results of the analytical model *Non-Compact* with results from an unsteady simulation and provided by the MOI model [13].

A. Test case 1: Kerosene-air inhomogeneities

1. Nozzle flow properties

Assuming one-dimensional and complete combustion at constant pressure, the mean burnt gases entering the nozzle are computed using the CANTERA library [22], the BFER two-step scheme for an equivalent modified $C_{10}H_{20}$ kerosene, and an intial air-kerosene mixture at an equivalence ratio of $\phi = 0.7$, $T = 300$ K and $p = 1$ bar. The mean burnt gas properties are provided in table 1. By setting small fluctuations of equivalent ratio around the mean equivalence ratio $\phi = 0.7$, the compositional fluctuations are estimated by differentiating the new burnt gas composition with the mean ones. These fluctuations are summarized in table 2 for an equivalence ratio fluctuation of $\hat{\phi} = 3.33 \cdot 10^{-3}$.

$\bar{T}$	$\bar{p}$	$\bar{Y}_{O_2}$	$\bar{Y}_{H_2O}$	$\bar{Y}_{CO}$	$\bar{Y}_{CO_2}$	$\bar{Y}_{N_2}$
1906 K	1 bars	0.0668	0.0584	$2e-4$	0.1424	0.7322

Table 1   Mean burnt gases

$\hat{\phi}$	$\hat{Y}_{O_2}$	$\hat{Y}_{H_2O}$	$\hat{Y}_{CO}$	$\hat{Y}_{CO_2}$	$\hat{Y}_{N_2}$
$\mp 3.33 \cdot 10^{-3}$	$\pm 373.3 \cdot 10^{-6}$	$\mp 133.3 \cdot 10^{-6}$	$\mp 6.7 \times 10^{-6}$	$\mp 313.3 \cdot 10^{-6}$	$\pm 80 \cdot 10^{-6}$

Table 2   Composition fluctuation amplitudes when $\phi = 0.7 \mp 3.33 \cdot 10^{-3}$

For this test case, the computational domain is shown in figure 1 and corresponds to the nozzle in [20]. The inlet total temperature and total pressure are 1966 K and 1.17 bars respectively, leading to an inlet Mach number of $M_{in} \simeq 0.48$. Thereafter, subsonic and choked flows are simulated by simply modifying the nozzle outlet pressure. In addition, the heat capacities of each species are set to constant to be consistent with the model in section III and are given in table 3.

2. Numerical set-up

17419 triangular cells are used to mesh the computational domain shown in figure 1. Furthermore, the final grid refinement allows capturing the pulse wave at the highest frequency $f = 6000$ Hz with 68 points using the second-order Lax-Wendroff convection scheme. The amplitudes of the compositional fluctuations pulsed at the inlet are given in table 2. At the end, a total simulation time of $T_{sim} = 0.1$ s is reached.

For post-processing, the waves are first computed as described by equation (13). Then, they are cross-sectional averaged at the inlet and outlet positions before computing the composition transfer functions as given by equation (22).

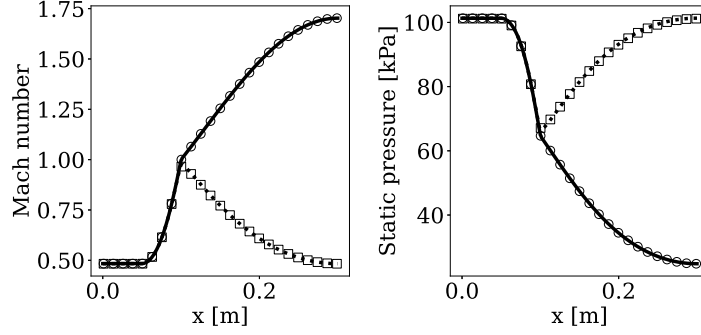| Species	O_2	H_2O	CO	CO_2	N_2
$C_{p,i}$ (J/kg/K)	1174.5	2832.4	1288.8	1365.3	1278.5

Table 3   Constant heat capacities

Fig. 2 **Cross-sectional averaged (a) Mach number and (b) static pressure profiles for both subsonic flow: 1D-model (······), AVBP (□) and choked flow: 1D-model (——), AVBP (○).**

3. Nozzle steady-mean flows

By imposing the outlet static pressure at different target values using the NSCBC methodology, different nozzle flow regimes are reached for similar inlet flows. For the subsonic flow, the pressure is relaxed through one atmosphere. On the contrary for the choked flow, no target is imposed at the nozzle outlet since the flow is supersonic.

Figure 2 compares the profiles of Mach number and static pressure along the nozzle between the cross-sectional profiles from the steady simulations and that from the one-dimensional solution. For both nozzle flow regimes, the Mach number and static pressure profiles from the analytical solution correspond well with that computed from the simulation. Thus, the quasi-one dimensional assumption of the nozzle flows is verified in both regimes.

4. Transfer function results : Subsonic nozzle

To obtain the composition transfer functions provided in equations (22), composition waves are pulsed through the choked nozzle flow. For the subsonic regime case, the *Non-Compact* solution is compared in figure 3 with the composition-to-acoustic transfer functions computed from the simulations. The acoustic transfer functions R^- and T^+ are predicted by the *Non-Compact* solution with less than 6% mean relative error compared to the numerical results.

Note that both analytical and numerical solutions predict a zero composition-to-entropy transfer function T^s. Indeed, according to equations (16c) and (16d), the invariants I_C and I_D are conserved and simply convected along the nozzle. Therefore, the amplitude of both invariants remains constant independently of the perturbation frequency. Moreover, assuming only composition fluctuations at the nozzle inlet and using the conservation equations (15c) and (15d) result in the following analytical formulation for the composition-to-entropy transfer functions noted T^s:

$$T^s = \log\left(\frac{2 + (\bar{\gamma} - 1)\bar{M}_{in}^2}{2 + (\bar{\gamma} - 1)\bar{M}_{out}^2}\right) \tag{23}$$
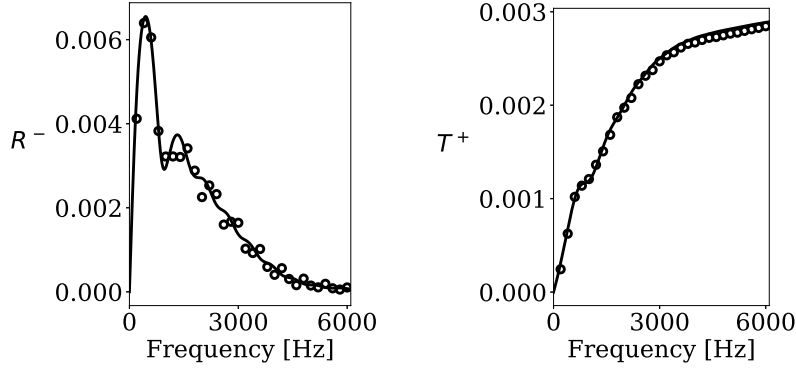
13

Fig. 3 Subsonic nozzle: (a) Modulus of the reflection acoustic transfer function R^- **(b) Modulus of the transmission acoustic transfer function** T^+ **.** *Non-Compact* **(——) , AVBP (○).**
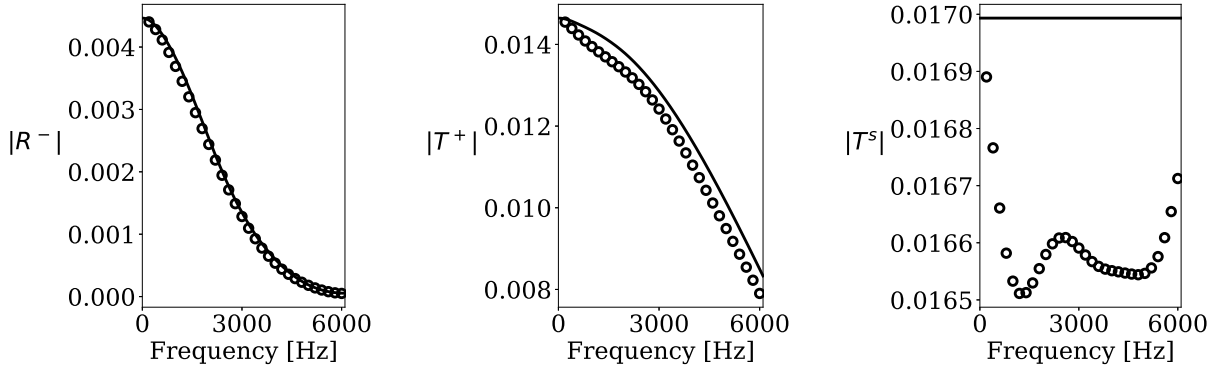

Fig. 4 Choked nozzle: (a) Modulus of the reflection acoustic transfer function. (b) Modulus of the transmission acoustic transfer function. (c) Modulus of the transmission composition-to-entropy transfer function. *Non-Compact* **(——) , AVBP (○).**

Therefore, in the particular case where $\bar{M}_{in} = \bar{M}_{out}$, the modulus of $|T^s|$ is indeed zero in addition to be independent of the frequency.

5. Transfer function results : Choked nozzle

Figure 4 shows the comparison of the composition-to-acoustic and composition-to-entropy transfer function results, noted R^-, T^+ and T^s, in terms of frequency between the unsteady simulation and the *Non-Compact* solution. At low frequency, $f \rightarrow 0$, the composition transfer functions R^-, T^+ and T^s converge to the simulation results. According to figure 4(a), the modulus of the reflection transfer functions R^- is retrieved by the one-dimensional solution *Non-Compact*. For the transmission transfer functions T^+ and T^s, the simulations results correspond to the analytical solution with less than 5.3% mean relative error.
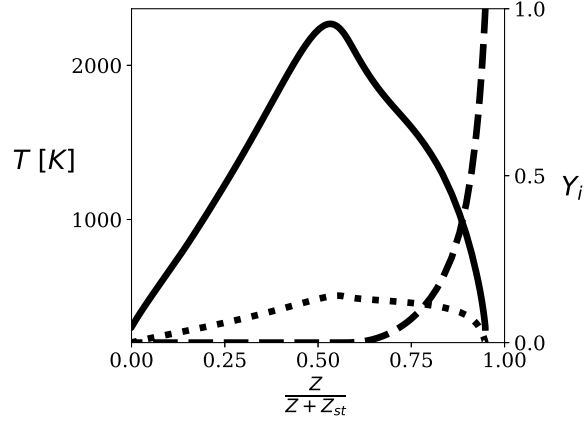
Fig. 5 One-dimensional pure-methane-air counter-flow diffusion flame. Temperature (——), Mass fraction of Y_{H_2O} (······), Mass fraction of Y_{CH_4} (- - -) profiles against the reduced mixture fraction space $\bar{Z}/(\bar{Z} + \bar{Z}_{st})$ where $\bar{Z}_{st}$ is the mean mixture fraction space at stochiometric condition.

$\bar{T}$	$\bar{p}$	$\bar{Y}_{O_2}$	$\bar{Y}_{H_2O}$	$\bar{Y}_{CO_2}$	$\bar{Y}_{N_2}$
1306 K	1×10^5 Pa	0.173	0.064	0.037	0.726

Table 4 Mean composition and temperature of the burnt gases

B. Test case 2: Methane-air inhomogeneities

1. Nozzle flow properties

The second test case relies on a one-dimensional counter-diffusion flame of methane-air according to [13], which is reproduced here and shown in figure 5. From the properties of this flame, the compositional fluctuations can be estimated by assuming small fluctuations of mixture fraction $\hat{Z}$ around a mean state defined at $\bar{Z} = 0.02$. Following [13], the mean burnt gas conditions entering the nozzle are taken at this mixture fraction space $\bar{Z} = 0.02$ and detailed in table 4 meanwhile the compositional fluctuations are given in table 5. For the mean inlet conditions, they are fixed to $T = 1306$ K and $p = 10^5$ Pa leading to an inlet total temperature of $T_t = 1323$ K and an inlet total pressure of $P_t = 105582$ Pa.

$\hat{Z}$	$\hat{Y}_{H_2O}$	$\hat{Y}_{CO_2}$	$\hat{Y}_{O_2}$	$\hat{Y}_{N_2}$
$\pm 3.33 \cdot 10^{-3}$	$\pm 8.33 \cdot 10^{-4}$	$\pm 7.67 \cdot 10^{-4}$	$\mp 14.33 \cdot 10^{-4}$	$\mp 1.67 \cdot 10^{-4}$

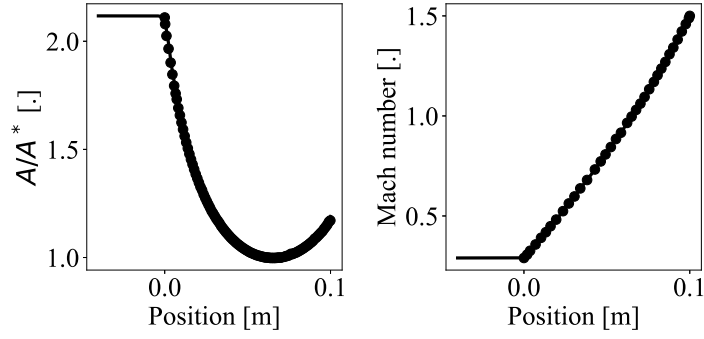**Table 5** Compositional fluctuations when $Z = 0.02 \pm 3.33 \cdot 10^{-3}$

Fig. 6   Dimensionless cross section profile A/A^* (left) and Mach profile along the nozzle (right). Original profile (○)) and Modelled (——).
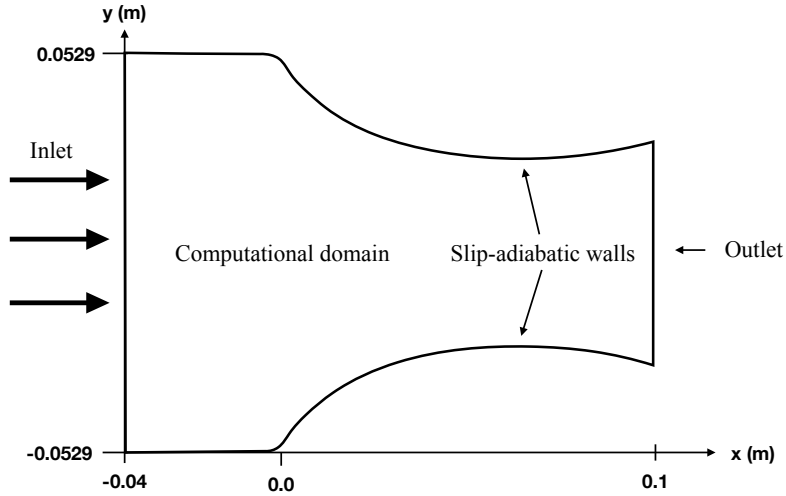

Fig. 7   Nozzle computational domain and boundary conditions.

2. Numerical set-up

The nozzle cross section profile, presented in figure 6 (left), is modelled to reproduce the Mach number profile given in figure 6 (right). 215200 triangle cells are used to discretize the nozzle, which resolves the highest frequency $f = 6000$ Hz with more than 30 points with the Lax-Wendroff convection scheme. Figure 7 presents the simulated computational domain and its associated boundary conditions. Furthermore, compositional fluctuations are pulsed at the inlet with amplitudes given in table 5.

A total simulation time of $T_{sim} = 0.1$ s is achieved. The constant heat capacities of the different species are given in table 6.

For post-processing, the fluctuating fields are computed before recasting them into waves as defined in equation (13). Afterward, the waves are cross-sectional averaged at the inlet positions where $M_{in} = 0.29$ and at the outlet positions where the Mach number is $M_{out} = 1.5$ (figure 6). In addition, the perturbation frequencies are expressed in Helmholtz

Species	O_2	H_2O	CO_2	N_2
$C_{p,i}$ (J/kg/K)	1125	2505.7	1298.5	1218.4

Table 6   Constant heat capacities

numbers instead: $\Omega = f L_n / c_0$.

3. Composition transfer functions

The composition-to-acoustic reflection R^-, the composition-to-acoustic transmission T^+, T^- and the composition-to-entropy transmission T^s transfer functions are shown in figure 8. Results from the simulation termed AVBP are compared with the *Non-Compact* analytical solution and with Magri's results [13]. Note that Magri's results for R^-, T^+ and T^- are first multiplied by a factor 2 in order to be consistent with the acoustic transfer function defined in section IV, before being arbitrarily divided by a factor $\kappa_1 = 60$ in order to yield the approximate order of magnitude of the AVBP simulation results. It can be emphasized here that no composition-to-entropy transmission transfer function T^s is provided by Magri [13], since this mechanism could not have been identified with his wave decomposition vector.

For the acoustic transfer functions, the predictions from the analytical solution *Non-Compact* and numerical solution AVBP converge at low frequencies, which is in agreement with theory [5]. On the contrary,

Magri's results [13] overestimate the compact coefficients by a factor κ_1 at least compared to the numerical solution AVBP.

Over the whole frequency range, while *Non-Compact* and AVBP reflection transfer function predictions R^- match well, a drastic and increasing gap in modulus is observed for T^+, T^- and T^s between *Non-Compact* and AVBP results. In fact, the cause of this increasing gap in the transmission transfer function is well known for entropy wave i.e. temperature fluctuations [2, 23–28]. A similar phenomenon impacts the composition waves since they propagate through the nozzle at the same convection speed $\bar{u}$ yielding a strong distortion of composition waves fronts as presented in figure 9 for the fluctuation of the species mass fractions of dioxygen noted $\hat{Y}_{O_2}$. Cross-averaging the waves at the outlet position in the simulation results in an overall decay due to the strong distortion of the composition wave fronts. Note that this phenomenon is not taken into account in the *Non-Compact* analytical solution, explaining the gap with the results AVBP in figure 8. Furthermore, the composition-to-composition transfer function $T^z = w_{out}^z / w_{in}^z$ between the nozzle inlet and outlet positions is computed from the simulation, presented in figure 10, and is used to correct the *Non-Compact* transmission transfer functions.

To do so, the modulus of the transmission transfer functions $|T^+|$, $|T^-|$ and $|T^s|$ are multiplied by the composition-to-composition transmission transfer functions $|T^z|$.

Consequently, the corrected results present a better match with respect to the frequency dependence of the simulation results, as presented in figure 8, confirming that two-dimensional effects are indeed responsible for the observed
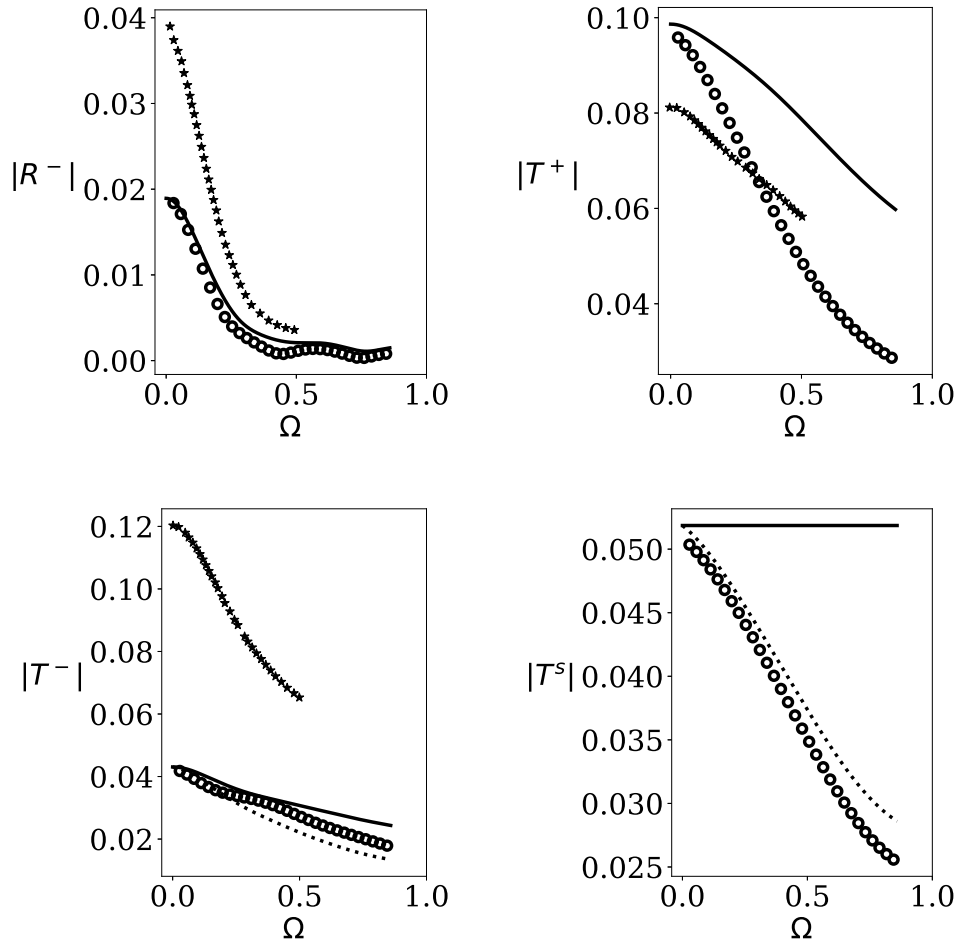
Fig. 8 **(Left-top) Composition-to-acoustic reflection transfer functions** R^-. **(Right-top) Composition-to-acoustic transmission transfer functions** T^+. **(Left-bottom) Composition-to-acoustic transmission transfer functions** T^-. **(Right-bottom) Composition-to-entropy transmission transfer functions** T^s. *Non-Compact* **(——),** **AVBP (○), Magri's results [13] divided by a factor** κ_1 **(⋆) and** *Non-Compact* **solution corrected with attenuation (⋯⋯).**
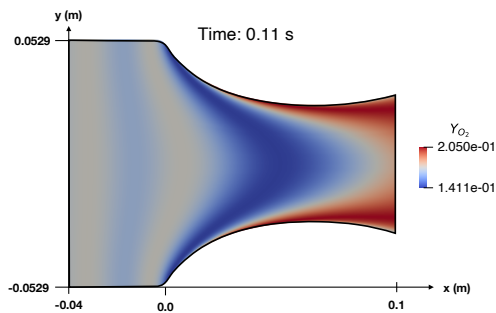
Fig. 9 **Instantaneous iso-contour of the composition fluctuation of the mass fraction species** $\hat{Y}_{O_2}$ **field within the nozzle.**
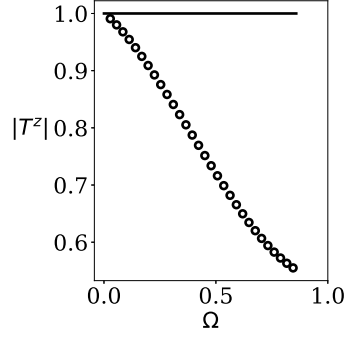
Fig. 10   Attenuation transfer function of composition wave. *Non-Compact* (——), AVBP (○).

discrepancies.

Compared to Magri's results [13], the acoustic transfer functions computed from the simulation are at least $\kappa_1 = 60$ times lower over the whole frequency range. As emphasized in Appendix A , the decomposition wave vector in [8, 13] is not a basis of independent variables since its entropy fluctuation $\hat{s}$ can be generated by compositional fluctuations $\hat{Y}_i$. Consequently, the composition-to-acoustic transfer functions in [13] do not account for the overall influence of compositional fluctuations since the entropy fluctuation $\hat{s}$ is forced to 0 when pulsing composition waves $\hat{Z}$. In this case, not accounting for the associated entropy wave caused by compositional fluctuations leads to overestimated compositional noise by a

factor κ_1.

VI. Application to a full-360° helicopter engine and parametric study on combustion noise generation through nozzle

A hybrid approach is considered thereafter to predict combustion noise from a full-360° helicopter engine. It consists of combining the LES results of a full-360° combustion chamber [2] one-way coupled to variable geometry nozzles. Downstream of the combustion chamber, the wave amplitude spectrum densities are extracted for the acoustic, the entropy and composition waves following the methodology described in [2], which is extended in this paper to composition waves. Afterward, a parametric study is performed on the nozzle geometries and thus the acoustic transmission transfer functions. Finally, combining both results, it is possible to investigate combustion noise and its breakdown depending on the different nozzle geometries.

A. Description of the full-360° combustion chamber simulation

Since Large Eddy Simulation (LES) allows capturing the acoustics and unsteadiness of the flow field with high accuracy, a full-360° reverse annular combustion chamber of the TEENI engine was simulated by Livebardon *et al.* [2],
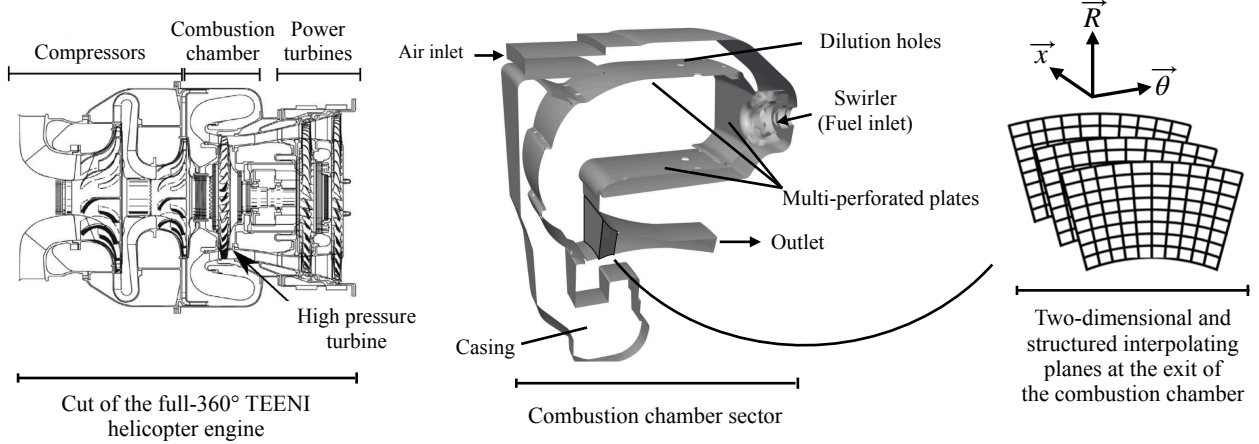
19

Fig. 11   Cut of the full-360° TEENI helicopter engine (left), combustion chamber sector (middle) and CHORUS interpolating mesh (right) [2].

presented in figure 11. The domain encompasses swirlers that create recirculation zones stabilizing the flame, some multi-perforated plates and dilution holes that cool down the burnt gases and protect the primary wall zone, and a nozzle at the exit of the combustion chamber to be representative of the sonic state of the stator enabling to reduce the computational cost. The operating point corresponds to an engine power equal to 900 kW [2].

The simulation is based on a full tetrahedral mesh composed of 110 million cells, sufficiently fine to propagate waves up to 5000 Hz, although the range of combustion noise is usually only up to 2000 Hz [2].

The BFER two-step chemistry scheme representative of the combustion of an equivalent modified $C_{10}H_{20}$ kerosene fuel is applied as well as the Dynamic Thickened Flame LES model, which further reduces the overall computational cost. In addition, the multi-perforated plates are modelled by specific acoustic impedance computed from an analytical solution obtained from the linearization of the Bernoulli equation [29].

At the end, T_{sim} = 43.2 ms of converged simulated physical time was performed with a CFL number of 0.7 [2].

B. Waves identification downstream of the combustion chamber

The process for wave identifications in heterogeneous species mixture flow is almost similar to that explained in [2] for homogeneous species mixture flow:

- After interpolating the flow properties over a mesh located downstream of the combustion chamber as sketched in figure 11(right), the flow fluctuations vector noted f' is computed, then radially-averaged and noted f'_R such that:

$$f'(x, R, \theta, t) \rightarrow f'_R(x, \theta, t)$$

Note that the entropy fluctuation is computed such that its definition corresponds to that provided in section III.

20

- The fluctuation vector f'_R is then decomposed using temporal Fourier transform in frequencies. The different azimuthal mode shapes, noted m, are then retrieved by decomposing the frequency signal vector using spatial Fourier transform over the azimuthal direction, yielding the vector $F'(x, m, f)$:

$$F'(x, m, f) = \frac{1}{2\pi} \int_0^{2\pi} \left(\frac{1}{T_{sim}} \int_0^{T_{sim}} f'_R(x, \theta, t) e^{-i\omega t} dt \right) e^{-im\theta} d\theta$$

- $F'(x, m, f)$ is then linked to the wave vector noted $W(x, m, f)$ through a passage matrix noted $[\mathbf{K}]$ (see [2] for more details) based on the dispersion relation derived from the two-dimensional Linearized Euler equations. Note that this matrix $[\mathbf{K}]$ is extended in multi-species flows with the following link between composition waves and compositional fluctuations: for any species i, $w_{Y_i} = \hat{Y}_i$.

$$W(x, m, f) = [\mathbf{K}] F'(x, m, f)$$

- Finally, the wave vector $W(x, m, f)$ is filtered at the end of the combustion chamber to extract only wave components with similar convection speed:

$$W_x(m, f) = \frac{1}{N_x} \sum_{i=1}^{N_x} W(x, m, f) e^{-iK_x x_i}$$

where K_x corresponds to the dimensionless axial wavenumber as defined in [2].

At the end, the full signal length T_{sim} is post-processed with a mean saving time step of $\Delta t = 0.13$ ms providing a frequency resolution up to 4000 Hz. The amplitude spectrum densities computed downstream of the combustion chamber for the acoustic, entropy and composition waves are given for the planar mode only in figure 12. Note that the species waves w_{CO} and w_{KERO} are dropped because they have a very low order of magnitude. In addition, it can be noticed that the species wave curves: w_{CO2}, w_{H2O}, w_{N2} and w_{O2} can be superimposed vertically using a constant multiplication factor for the whole frequency range.

C. Parametric studies on the transfer functions

Following the study in [30], the nozzle geometry is parametrized as presented in figure 13. The flow properties entering at the nozzle inlet are fixed by the ones found downstream of the combustion chamber, in particular the ones computed on the last axial interpolated mesh. In addition, the nozzle inlet section is fixed to the turbine section found on the last axial interpolated mesh, involving a single nozzle radius noted R_{in}.

Similarly to the simulation of Livebardon *et al.* [2] where a choked nozzle is used for the outlet boundary condition, a choked nozzle is investigated here involving a unique possible throat section according to the conservation equation of
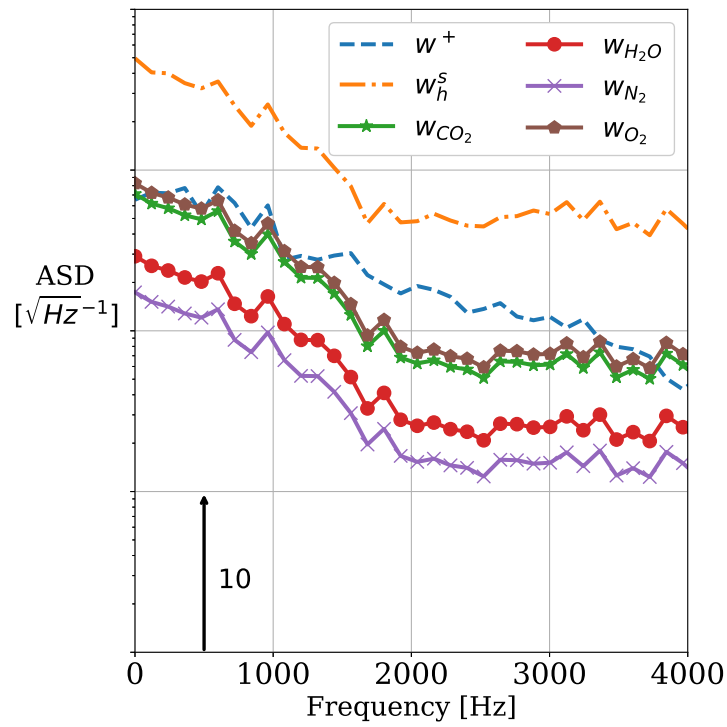
Fig. 12 Amplitude spectrum densities of the non-dimensioned acoustic w^+, entropy w_h^s and species waves w_k computed downstream of the full-360° combustion chamber
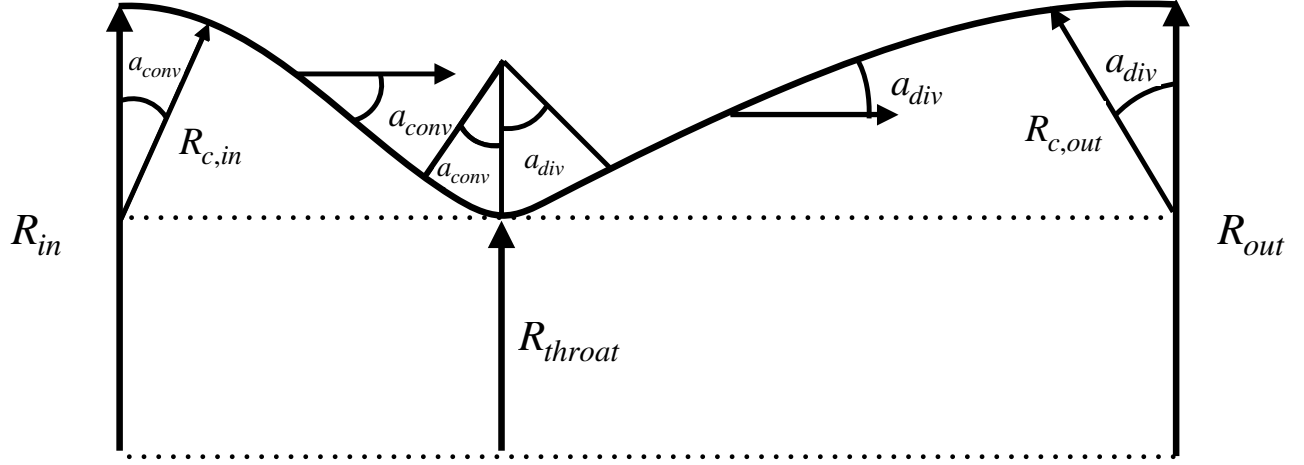
Fig. 13   Nozzle parametric description [30].

Species	O_2	H_2O	CO_2	N_2
$\bar{Y}_i$	0.1434	0.0315	0.0769	0.7482
dY_i/dY_{O_2}	1.	-0.35	-0.86	0.21

Table 7   Mean species mixture composition $\bar{Y}_i$ and first order derivatives dY_i/dY_{O2}

the mass-flow rate. As a result, it leads to a unique nozzle throat radius noted R_{throat} and a single inlet curvature radius noted $R_{c,in}$ since it is defined such that: $R_{c,in} = R_{in} - R_{throat}$. The only left unknown parameter is the angle of the convergent noted a_{conv} . By varying the Mach number noted M_{out} at the outlet nozzle, different sections are obtained using the conservation of the mass-flow rate. This leads for one fixed M_{out} to a unique nozzle outlet radius noted R_{out} and a unique outlet curvature radius $R_{c,out}$ since it is defined as: $R_{c,out} = R_{out} - R_{throat}$. Therefore, the only left unknown parameter within the divergent nozzle is the angle noted a_{div}. Thus, the nozzle is parameterized with three variables: the angle a_{conv} of the convergent nozzle, the angle a_{div} of the divergent nozzle and the outlet Mach number M_{out} .

For the computation of the composition transfer function and according to section III, all the species waves are expressed arbitrarily in terms of the dioxygen species wave w_{O_2} such that:

$$w_i = \frac{dY_i}{dY_{O_2}} w_{O_2}, \qquad \text{where} \qquad \frac{dY_i}{dY_{O_2}} = \frac{\hat{Y}_i}{\hat{Y}_{O_2}}. \tag{24}$$

As a result, the mean species mass-fractions computed downstream of the combustion chamber and the first order derivatives for the different species waves are given in table 7

By varying the angles a_{conv} and a_{div} from 3° to 30° and the outlet Mach number M_{out} from 1.1 to 2., different nozzle geometries are generated. Finally, the *Non-Compact* acoustic transmission transfer functions are then computed

for each type of incident waves, entropy, acoustic and composition for frequency up to 4000 Hz.

The acoustic transmission transfer functions for varying M_{out}, a_{conv}, a_{div} and incident waves at a fixed frequency $f = 840$ Hz, are compared in figures 14 and 15.

In the following, note that the composition-to-acoustic, entropy-to-acoustic and acoustic-to-acoustic transmission transfer functions are computed and noted: $T_z^+ = w_{out}^+/w_{in}^z$, $T_s^+ = w_{out}^+/w_{in}^s$, $T_+^+ = w_{out}^+/w_{in}^+$, $T_z^- = w_{out}^-/w_{in}^z$, $T_s^- = w_{out}^-/w_{in}^s$ and $T_+^- = w_{out}^-/w_{in}^+$.

All acoustic transmission transfer functions are hardly sensitive to the variation of a_{div}, except at very low a_{div}, whereas the dependency on a_{conv} is more important. In addition, the higher the outlet Mach number M_{out} is, the higher the transmission composition-to-acoustic and entropy-to-acoustic transfer functions are. Note here that the attenuation of entropy and composition waves is not accounted for whereas it plays a major role in acoustic transmission prediction.
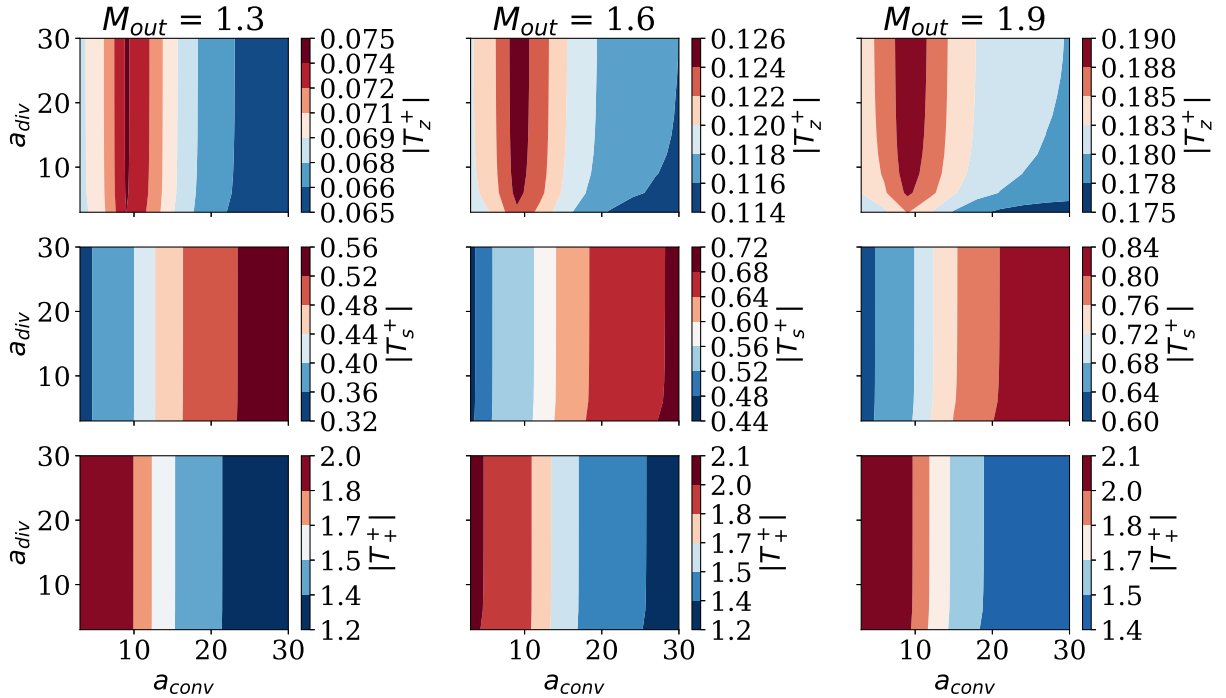

Fig. 14 **Acoustic transmission transfer functions T_z^+, T_s^+ and T_+^+ for fixed frequency $f = 840$ Hz**

In contrast, figure 16 presents the resulting acoustic (w^-) transmission transfer function modulus for the different incident waves at the frequency of $f = 120$ Hz. These results show differences with the ones computed at $f = 840$ Hz in figure 15 and highlights that non-compact effects are also involved in the transfer functions modulus variation.

a_{div} is then arbitrarily fixed to $12°$. The acoustic transmission transfer functions modulus (w_{out}^+) for the different incident waves, three outlet Mach numbers M_{out} and various a_{conv} are shown as a function of frequencies in figure 17.
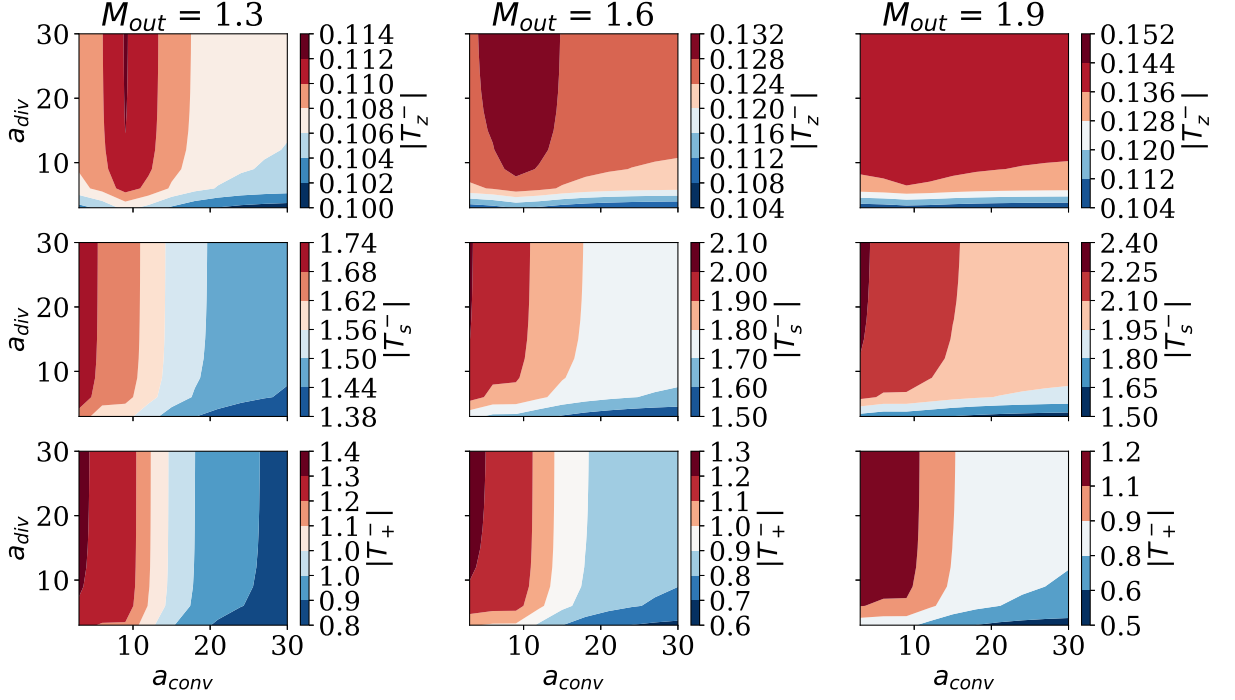
Fig. 15   Acoustic transmission transfer functions T_z^-, T_s^- and T_+^- for fixed frequency $f = 840$ Hz

According to these results, the composition-to-acoustic T_z^+, the entropy-to-acoustic T_s^+ and the acoustic-to-acoustic transfer functions T_+^+ all show significant variations with frequency and the angle a_{conv} . Even though they all increase in magnitude over the whole frequency range with an increase of M_{out} , T_+^+ is less sensitive than the others transfer functions.

D. Combustion noise parametric study

By combining the wave amplitude spectrum densities and their transmission transfer functions, the dimensionless acoustic amplitude spectrum densities (AASD) generated downstream of the nozzle due to each type of waves are predicted. The pressure amplitude spectrum density (PASD) is then deduced by summing the AASD of both acoustic wave w^+ and w^- and dividing the product by two.

The sound power spectrum density (SPSD) is then deduced by multiplying the square of the PASD with $\bar{\gamma}\bar{c}\bar{p}$. The acoustic intensity levels in dB/Hz noted $I_{dB/Hz}$ are then computed for each different frequencies as well as the total acoustic intensity levels noted I_{dB} such that:

$$I_{dB/Hz}(f) = 10 \log_{10}\left(\frac{SPSD}{W_{ref}}\right) \qquad \text{and} \qquad I_{dB} = 10 \log_{10}\left(\frac{\int_{f_0}^{f_{max}} SPSD(f)df}{W_{ref}}\right) \qquad (25)$$
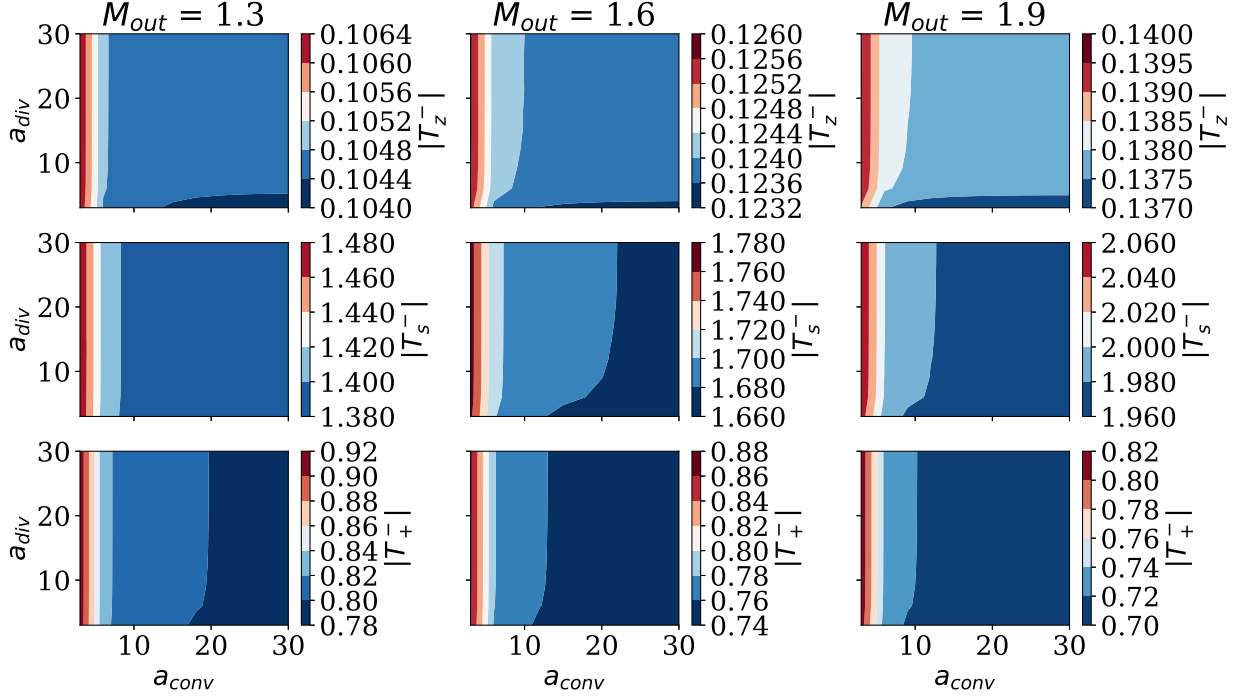
Fig. 16 Acoustic transmission transfer functions T_z^-, T_s^- and T_+^- for fixed frequency $f = 120$ **Hz**

where $W_{ref} = 10^{-12}$ W is the reference sound power computed at the threshold of hearing at 1kHz for a typical human ear.

Although the transmission transfer functions vary with a_{conv} and M_{out}, the difference in terms of acoustic intensity levels in decibels for the different frequencies are quite small for each of the different contributions. Therefore, by fixing $a_{conv} = a_{div} = 12°$ and $M_{out} = 1.3$, figure 18 compares the different noise levels for the different perturbation frequencies. The indirect composition noise is at least 20 dB lower than direct noise and indirect entropy noise.

Finally, figure 19 compares the total acoustic intensity levels in decibels integrated over frequencies for direct, indirect entropy and indirect composition noise with their a_{conv}- and M_{out}-dependence. The levels of composition noise are at least 20 dB lower than the levels of direct noise or indirect entropy noise. It is interesting to note also that the higher the outlet Mach number is, the lower the direct noise mechanism and the higher the indirect composition noise are.

VII. Conclusion

The definition of compositional and entropy noise for multi-species flows has been revisited in the context of multi-species mixture flows. This re-examination relies on the separation of the linearized specific entropy s'/C_p into contributions related to the specific entropy fluctuations of each pure species given by $\hat{s}_n$ and to the i-th species mass
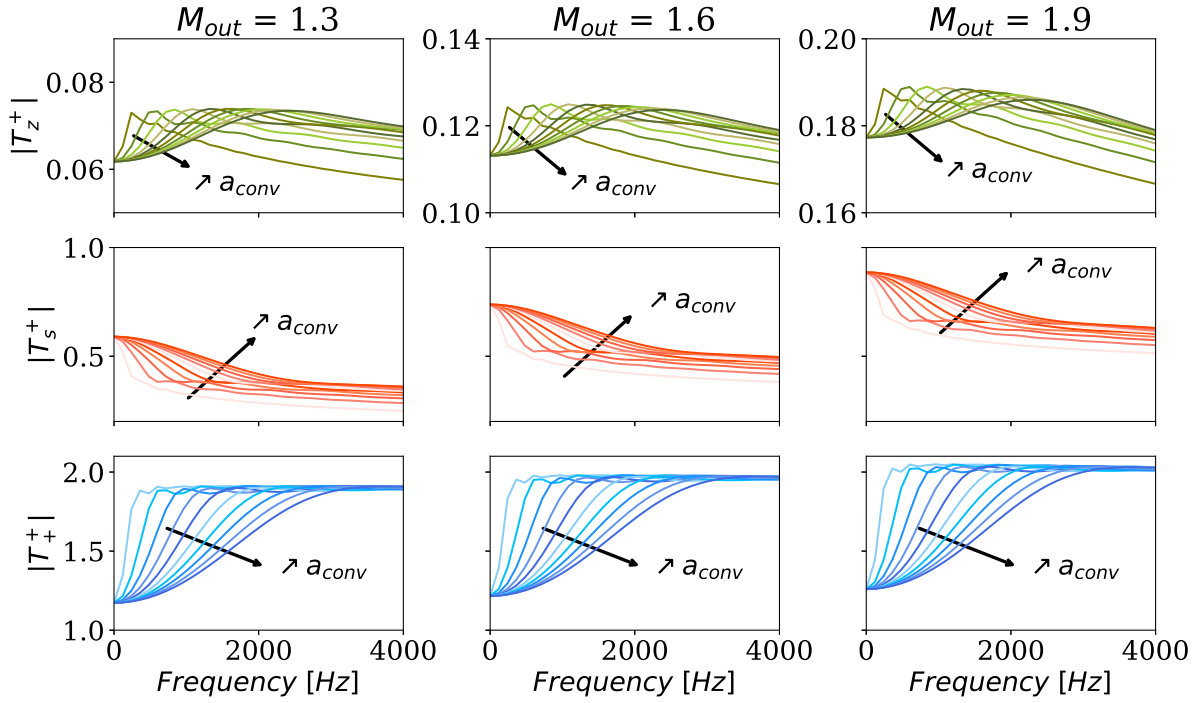
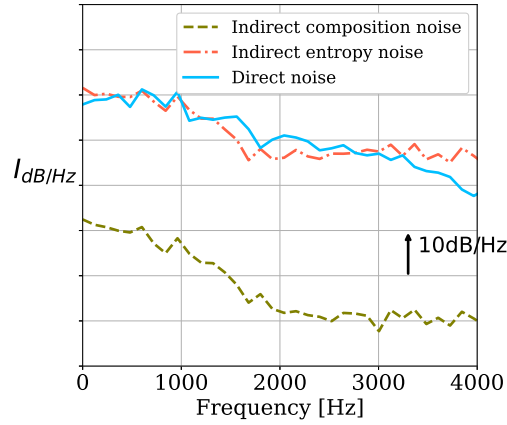**Fig. 17   Acoustic transmission transfer functions** T_z^+, T_s^+ **and** T_+^+

Fig. 18   Noise breakdown downstream of the nozzle for $a_{conv} = a_{div} = 12°$ **and** $M_{out} = 1.3$ **and various frequencies**

fractions fluctuations $\hat{Y}_i$. While entropy noise is caused by the acceleration of the entropy wave properly defined by $\hat{s}_n$, composition-noise mechanism is brought about by the acceleration of the species mass fractions fluctuations noted $\hat{Y}_i$ or equivalently the mixture fraction space fluctuations $\hat{Z}$.

A new one-way coupling between composition and entropy waves has been exhibited when considering quasi-
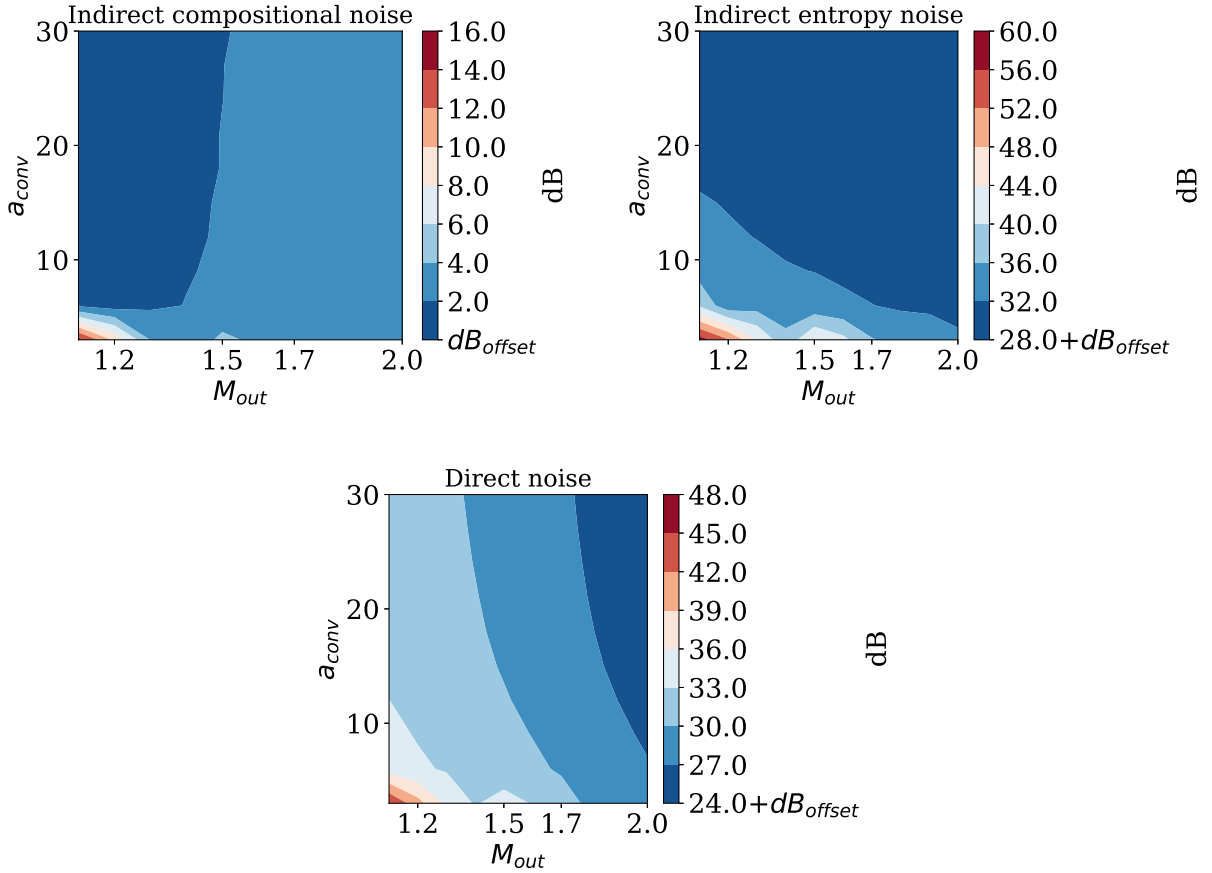
Fig. 19 Total noise breakdown downstream of the nozzle with α-dependence and M_{out}-dependence for $a_{div} = 12°$

one-dimensional flow in nozzles. Relying on the Magnus expansion, an exact solution for the quasi-one-dimensional linearized Euler equations has been studied. Thanks to the extension of the Navier Stokes Characteristics Boundary Conditions to multi-species flow, which enables the entropy wave to be defined correctly $w_h^s = \hat{s}_n$, the improved model has been validated against direct numerical simulations of nozzle flows.

Finally, in order to investigate the contribution of the composition wave to the indirect combustion noise, a parametric study has been performed on a real helicopter engine. The different waves from the full-360° combustion chamber have been extracted and propagated. The results show that compositional noise is negligible compared with indirect entropy noise and direct noise in all the cases considered.

Appendix A. Differences with the MOI model

The differences with the MOI model [13] are two-folds.

First difference. The first difference comes from the linearization and integration of the Gibbs' energy equation (2) linking the entropy fluctuation $\hat{s}$ to other fluctuations. To do so, let's start from the differential equation (2.7) in [13] obtained in the Magri *et al.* model given in the following by:

$$\frac{\mathrm{d}s}{C_p} = \frac{\mathrm{d}p}{\gamma p} - \frac{\mathrm{d}\rho}{\rho} - (\psi + \aleph)\,\mathrm{d}Z \tag{A1}$$

where:

$$\aleph = \sum_{i=1}^{N} \left(\frac{1}{(\gamma - 1)} \frac{\mathrm{d}\log(\gamma)}{\mathrm{d}Y_i} + \frac{T^\circ}{T} \frac{\mathrm{d}\log(C_p)}{\mathrm{d}Y_i} \right) \frac{\mathrm{d}Y_i}{\mathrm{d}Z} \tag{A2a}$$

$$\psi = \frac{1}{C_p T} \sum_{i=1}^{N} \frac{\mu_i}{W_i} \frac{\mathrm{d}Y_i}{\mathrm{d}Z} \tag{A2b}$$

When linearizing the equation (A1), it is obtained that:

$$\mathrm{d}\left(\hat{s} - \hat{p} + \hat{\rho}\right) = \underbrace{-\left(\bar{\psi} + \bar{\aleph}\right)\mathrm{d}\hat{Z}}_{(1)} - \underbrace{\frac{\hat{\gamma}\,\mathrm{d}\bar{p}}{\bar{\gamma}\,\bar{\gamma}\,\bar{p}}}_{(2)} \tag{A3}$$

Thereafter, the second righ-hand term (2) in equation (A3) can be recast as proposed in [13] such that:

$$-\frac{\hat{\gamma}\,\mathrm{d}\bar{p}}{\bar{\gamma}\,\bar{\gamma}\,\bar{p}} = -\mathrm{d}\left(\bar{\phi}\hat{Z}\right) \quad \text{where} \quad \bar{\phi} = \frac{\mathrm{d}\log(\bar{\gamma})}{\mathrm{d}Z}\log\left(\bar{p}^{1/\bar{\gamma}}\right) \tag{A4}$$

Note here that by combining mean flow equation (4), a more convenient factor can be obtained depending on the Mach number $\bar{M}$ instead of the pressure:

$$-\frac{\hat{\gamma}\,\mathrm{d}\bar{p}}{\bar{\gamma}\,\bar{\gamma}\,\bar{p}} = \mathrm{d}\left(\bar{\phi}_2\hat{Z}\right) \quad \text{where} \quad \bar{\phi}_2 = \log(2 + (\bar{\gamma} - 1)\bar{M}^2)\left[\sum_{i=1}^{N}\left(\frac{\bar{W}}{W_i} - \frac{\bar{C}_{p,i}}{\bar{C}_p}\right)\frac{\mathrm{d}Y_i}{\mathrm{d}Z}\right] \tag{A5}$$

For the first term (1) in the right of equation (A3), it is proposed in the Magri *et al.* model [13] that:

$$-\left(\bar{\psi} + \bar{\aleph}\right)\mathrm{d}\hat{Z} = -\mathrm{d}\left[\left(\bar{\psi} + \bar{\aleph}\right)\hat{Z}\right] \quad \text{yielding} \quad \hat{s} = \hat{p} - \hat{\rho} - \left(\bar{\psi} + \bar{\aleph} + \bar{\phi}\right)\hat{Z} \tag{A6}$$

Assuming that the temperature of reference $T^\circ = 0$ K, it is obtained that the coefficient $\bar{\aleph}$ is constant along the nozzle such that: $\hat{Z}\mathrm{d}(\bar{\aleph}) = 0$. Nevertheless, the coefficient $\bar{\psi}$

varies

along the nozzle and the equation (A6) needs to be extended by an additional term such that:

$$- \left(\bar{\psi} + \bar{\aleph} \right) \mathrm{d}\hat{Z} = -\mathrm{d}\left[\left(\bar{\psi} + \bar{\aleph} \right) \hat{Z} \right] + \sum_{i=1}^{N} \hat{Y}_i \mathrm{d}\left(\frac{1}{\bar{C}_p \bar{T}} \frac{\bar{\mu}_i}{W_i} \right) \tag{A7}$$

According to [13], the chemical potential of the i-th species is given by:

$$\bar{\mu}_i = \bar{\mu}_i^\circ + \mathcal{R}_u \bar{T} \log \left(\bar{X}_i \frac{\bar{p}}{p^\circ} \right) \tag{A8}$$

Assuming $T^\circ = 0$ K involves that: $\bar{\mu}_i^\circ = 0$, introducing this result and equation (A8) within equation (A7) gives:

$$\sum_{i=1}^{N} \hat{Y}_i \mathrm{d}\left(\frac{1}{\bar{C}_p \bar{T}} \frac{\bar{\mu}_i}{W_i} \right) = \sum_{i=1}^{N} \hat{Y}_i \mathrm{d}\left(\frac{1}{\bar{C}_p} \frac{\mathcal{R}_u}{W_i} \log\left(\bar{p} \right) \right) = \frac{(\bar{\gamma} - 1)}{\bar{\gamma}} \sum_{i=1}^{N} \mathrm{d}\left(\frac{r_i}{r} \log\left(\bar{p} \right) \right) \hat{Y}_i = \mathrm{d}\left[\bar{\phi}_3 \hat{Z} \right] = \mathrm{d}\left[\bar{\phi}_4 \hat{Z} \right] \tag{A9}$$

where:

$$\bar{\phi}_3 = \frac{(\bar{\gamma} - 1)}{\bar{\gamma}} \log\left(\bar{p} \right) \sum_{i=1}^{N} \frac{W}{W_i} \frac{\mathrm{d}Y_i}{\mathrm{d}Z} \quad \text{and} \quad \bar{\phi}_4 = -\log\left(2 + (\bar{\gamma} - 1)\bar{M}^2 \right) \sum_{i=1}^{N} \frac{W}{W_i} \frac{\mathrm{d}Y_i}{\mathrm{d}Z} \tag{A10}$$

Note that it can be shown using mean flow equations (4) that $\mathrm{d}\bar{\phi}_3 = \mathrm{d}\bar{\phi}_4$ and thus that: $\mathrm{d}\left[\bar{\phi}_3 \hat{Z} \right] = \mathrm{d}\left[\bar{\phi}_4 \hat{Z} \right]$.

Assembling all the terms and integrating it from a reference state ($T^\circ = 0$ K, $p^\circ = 1$ bar), one less term and an additional

term $\bar{\phi}_3 \hat{Z}$ (or $\bar{\phi}_4 \hat{Z}$) compared to the equation (A6) are obtained:

$$\hat{s} = \hat{p} - \hat{\rho} - \left(\bar{\psi} + \bar{\phi} - \bar{\phi}_3 \right) \hat{Z} \tag{A11}$$

To sum up, the definition of the specific entropy fluctuation $\hat{s}$ used in the Magri *et al.* model [13] is incomplete as it lacks a term and keeps one term that should vanish in the assumption of $T^\circ = 0$ K.

Second difference. The second difference concerns the wave decomposition vector. As demonstrated in equation (A11), the entropy wave defined through the fluctuation $w^s = \hat{s}$ is dependent on the composition wave $w^z = \hat{Z}$. This implies that to account for the overall impact of composition wave when pulsing these through a nozzle inlet, it is required to pulse also its associated entropy wave w^s. Nevertheless, when computing composition-to-acoustic transfer functions through the nozzle, composition waves are often pulsed through the inlet meanwhile forcing all the other in-going waves to zero, including the entropy wave w^s. In the Magri *et al.* model [13], the following dependent wave decomposition vector is used $[w^+, w^-, w^s = \hat{s}, w^z = \hat{Z}]$. To avoid this problem, a more convenient wave decomposition vector is

proposed here and is given by $[w^+, w^-, w_h^s = \hat{s}_n, w^z]$ following equation results (12 and 13). Consequently, with this independent wave decomposition vector, the overall influence of composition waves can be accessed and is about to be verified thereafter with unsteady nozzle simulations.

Appendix B. Extension of Navier-Stokes Characteristics Boundary Conditions to multi-species flow

As proposed by [31], the Navier-Stokes Characteristics Boundary Conditions methodology (NSCBC) consists of decomposing flow variables at the boundary condition into a system of waves. This wave system encompasses one entropy wave noted $\mathcal{L}_2$, two vorticity waves noted $\mathcal{L}_3$ and $\mathcal{L}_4$, two acoustic waves noted $\mathcal{L}_1$ and $\mathcal{L}_5$ and N_i species waves noted $\mathcal{L}_{i+5}$ for the i-th species in a three-dimensional flow. Depending on the flow nature (subsonic or supersonic) and boundary position (inlet or outlet), some waves are either ingoing or outgoing. While the outgoing waves are computed directly from the domain, the ingoing waves are prescribed such that it respects some mean flow targets and pulsed signals under the assumption of Localized One-Dimensional Inviscid flow (LODI) as further detailed in [31]. This decomposition is correct for homogeneous mixture flow (i.e. $Y_i' = 0$) and the definition of the entropy wave $\mathcal{L}_2$ is given by equation (B1):

$$\mathcal{L}_2 = u \left(c^2 \frac{\partial \rho}{\partial x} - \frac{\partial p}{\partial x} \right) \tag{B1}$$

Nevertheless, this definition of the entropy wave through the excess-density wave (equation (B1) is dependent on the species waves in multi-species flow as it can be recast in the following form:

$$\mathcal{L}_2 = u \left((\gamma - 1) \frac{\partial p}{\partial x} - \frac{\gamma p}{T} \frac{\partial T}{\partial x} + \gamma p \sum_{i=1}^{N_i} \frac{r_i}{r} \mathcal{L}_{i+5} \right) \quad \text{where} \quad \mathcal{L}_{i+5} = -\frac{\partial Y_i}{\partial x} \tag{B2}$$

Thus, when pulsing composition waves $\mathcal{L}_{i+5}$ at constant pressure and temperature, the entropy wave strength $\mathcal{L}_2$ is non-zero according to equation (B2), which is an issue.

To avoid this problem, the entropy wave $\mathcal{L}_2$ can be defined similarly as for the entropy wave noted $w_h^s = \hat{s}_n$. To do so, the right-hand term in equation (B2) linked to the $\mathcal{L}_{i+5}$ needs to be added to the equation (B1). Consequently, the entropy wave $\mathcal{L}_2$ becomes now independent of the species waves and reads:

$$\mathcal{L}_2 = u \left(c^2 \frac{\partial \rho}{\partial x} + \rho c^2 \sum_{i=1}^{N} \frac{r_i}{r} \frac{\partial Y_i}{\partial x} + \frac{\partial p}{\partial x} \right) = -u \left[\frac{\gamma p}{T} \frac{\partial T}{\partial x} + (1 - \gamma) \frac{\partial p}{\partial x} \right] \tag{B3}$$

By adding this modification within the NSCBC methodology, it is now possible to pulse composition waves without producing entropy and acoustic waves.

Acknowledgments

References

[1] Morgans, A. S., and Duran, I., "Entropy noise: A review of theory, progress and challenges," *International Journal of Spray and Combustion Dynamics*, Vol. 8, No. 4, 2016, pp. 285–298. https://doi.org/10.1177/1756827716651791.

[2] Livebardon, T., Moreau, S., Gicquel, L., Poinsot, T., and Bouty, E., "Combining LES of combustion chamber and an actuator disk theory to predict combustion noise in a helicopter engine," *Combustion and Flame*, Vol. 165, 2016, pp. 272–287. https://doi.org/10.1016/j.combustflame.2015.12.012.

[3] Férand, M., Livebardon, T., Moreau, S., and Sanjosé, M., "Numerical Prediction of Far-Field Combustion Noise from Aeronautical Engines," *Acoustics*, Vol. 1, No. 1, 2019, pp. 174–198. https://doi.org/10.3390/acoustics1010012.

[4] Marble, F. E., and Candel, S. M., "Acoustic disturbance from gas non-uniformities convected through a nozzle," *Journal of Sound and Vibration*, Vol. 55, No. 2, 1977, pp. 225–243. https://doi.org/10.1016/0022-460X(77)90596-X.

[5] Duran, I., and Moreau, S., "Solution of the quasi-one-dimensional linearized Euler equations using flow invariants and the Magnus expansion," *Journal of Fluid Mechanics*, Vol. 723, 2013, pp. 190–231. https://doi.org/10.1017/jfm.2013.118.

[6] Hirschberg, L., Hulshoff, S. J., and Bake, F., "Sound production due to Swirl–Nozzle interaction: Model-based analysis of experiments," *AIAA Journal*, Vol. 59, No. 4, 2021, pp. 1269–1276. https://doi.org/10.1016/j.jsv.2018.09.011.

[7] Hirschberg, L., Bake, F., Knobloch, K., Hulshoff, S. J., and Hirschberg, A., "Experimental investigations of indirect noise due to modulation of axial vorticity and entropy upstream of a choked nozzle," *Journal of Sound and Vibration*, Vol. 532, 2022, p. 116989. https://doi.org/10.1016/j.jsv.2018.09.011.

[8] Magri, L., O'Brien, J., and Ihme, M., "Compositional inhomogeneities as a source of indirect combustion noise," *Journal of Fluid Mechanics*, Vol. 799, 2016. https://doi.org/10.1017/jfm.2016.397.

[9] Ihme, M., "Combustion and Engine-Core Noise," *Annual Review of Fluid Mechanics*, Vol. 49, No. August, 2017, pp. 277–310. https://doi.org/10.1146/annurev-fluid-122414-034542.

[10] Shao, C., Maeda, K., and Ihme, M., "Analysis of core-noise contributions in a realistic gas-turbine combustor operated near lean blow-out," *Proceedings of the Combustion Institute*, Vol. 000, 2020, pp. 1–9. https://doi.org/10.1016/j.proci.2020.07.078.

[11] Giusti, A., Magri, L., and Zedda, M., "Flow Inhomogeneities in a Realistic Aeronautical Gas-Turbine Combustor: Formation, Evolution, and Indirect Noise," *Journal of Engineering for Gas Turbines and Power*, Vol. 141, No. 1, 2019, pp. 1–11. https://doi.org/10.1115/1.4040810.

[12] Lapeyre, C., "Etude numérique de la stabilité, la stabilisation et le bruit de flamme dans un bruleur tourbillonnaire en conditions amorcées," Ph.D. thesis, Institut National Polytechnique de Toulouse (INP Toulouse), 2015.

[13] Magri, L., "On indirect noise in multicomponent nozzle flows," *Journal of Fluid Mechanics*, Vol. 828, 2017, pp. 1–14. https://doi.org/10.1017/jfm.2017.591.

[14] Shao, C. X., and Ihme, M., "Effect of operating conditions on core noise for a realistic gas-turbine combustor," *Center for Turbulence Research Annual Research Briefs 2020*, 2020.

[15] Blanes, S., Casas, F., Oteo, J. A., and Ros, J., "The Magnus expansion and some of its applications," *Physics Reports*, Vol. 470, No. 5-6, 2009, pp. 151–238. https://doi.org/10.1016/j.physrep.2008.11.001.

[16] Livebardon, T., "Modélisation du bruit de combustion dans les turbines d'hélicoptères," Ph.D. thesis, Institut National Polytechnique de Toulouse (INP Toulouse), 2015.

[17] Bailly, C., Bogey, C., and Candel, S., "Modelling of Sound Generation by Turbulent Reacting Flows," *International Journal of Aeroacoustics*, Vol. 9, No. 4-5, 2010, pp. 461–489. https://doi.org/10.1260/1475-472x.9.4-5.461.

[18] DeHoff, R. T., *Thermodynamics in Material Science*, McGraw-Hill, 1993.

[19] Cumpsty, N. A., and Marble, F. E., "Interaction of Entropy Fluctuations With Turbine Blade Rows; a Mechanism of Turbojet Engine Noise." *Proc R Soc London Ser A*, Vol. 357, No. 1690, 1977, pp. 323–344. https://doi.org/10.1098/rspa.1977.0171.

[20] Goh, C. S., and Morgans, A. S., "Phase prediction of the response of choked nozzles to entropy and acoustic disturbances," *Journal of Sound and Vibration*, Vol. 330, No. 21, 2011, pp. 5184–5198. https://doi.org/10.1016/j.jsv.2011.05.016.

[21] Schønfeld, T., and Rudgyard, M., "Steady and unsteady flow simulations using the hybrid flow solver AVBP," *AIAA journal*, Vol. 37, No. 11, 1999, pp. 1378–1385.

[22] Goodwin, D. G., Speth, R. L., Moffat, H. K., and Weber, B. W., "Cantera: An Object-oriented Software Toolkit for Chemical Kinetics, Thermodynamics and Transport Processes," https://www.cantera.org, 2021. https://doi.org/10.5281/zenodo.4527812, version 2.5.1.

[23] Morgans, A. S., Goh, C. S., and Dahan, J. A., "The dissipation and shear dispersion of entropy waves in combustor thermoacoustics," *Journal of Fluid Mechanics*, Vol. 733, 2013, pp. R2:1–10. https://doi.org/10.1017/jfm.2015.730.

[24] Leyko, M., Duran, I., Moreau, S., Nicoud, F., and Poinsot, T., "Simulation and Modelling of the waves transmission and generation in a stator blade row in a combustion-noise framework," *Journal of Sound and Vibration*, Vol. 333, No. 23, 2014, pp. 6090–6106. https://doi.org/10.1016/j.jsv.2014.06.034.

[25] Bauerheim, M., Duran, I., Livebardon, T., Wang, G., Moreau, S., and Poinsot, T., "Transmission and reflection of acoustic and entropy waves through a stator–rotor stage," *Journal of Sound and Vibration*, Vol. 374, 2016, pp. 260–278. https://doi.org/10.1016/j.jsv.2016.03.041.

[26] Giusti, A., Worth, N. A., Mastorakos, E., and Dowling, A. P., "Experimental and numerical investigation into the propagation of entropy waves," *AIAA Journal*, Vol. 55, No. 2, 2017, pp. 446–458. https://doi.org/10.2514/1.J055199.

[27] Fattahi, A., Hosseinalipour, S. M., and Karimi, N., "On the dissipation and dispersion of entropy waves in heat transferring channel," *Physics of Fluids*, Vol. 29, No. 8, 2017, pp. 087104:1–17. https://doi.org/10.1016/S0022-460X(70)80038-4.

[28] Emmanuelli, A., Zheng, J., Huet, M., Giauque, A., Le Garrec, T., and Ducruix, S., "Description and application of a 2D-axisymmetric model for entropy noise in nozzle flows," *Journal of Sound and Vibration*, Vol. 472, 2020, p. 115163. https://doi.org/10.1016/j.jsv.2019.115163.

[29] Mendez, S., and Eldredge, J. D., "Acoustic modeling of perforated plates with bias flow for Large-Eddy Simulations," *Journal of Computational Physics*, Vol. 228, No. 13, 2009, pp. 4757–4772. https://doi.org/10.1016/j.jcp.2009.03.026.

[30] Bell, W. A., Daniel, B. R., and Zinn, B. T., "Experimental and theoretical determination of the admittances of a family of nozzles subjected to axial instabilities," *Journal of Sound and Vibration*, Vol. 30, No. 2, 1973, pp. 179–190. https://doi.org/10.1016/S0022-460X(73)80112-9.

[31] Poinsot, T., and Veynante, D., *Theorical and Numerical Combustion*, 3rd ed., 2012.